SUBMISSION TO TUNNELLING AND UNDERGROUND SPACE TECHNOLOGY

TUST_2019_157R2

FIRST SUBMISSION: 06 February 2019

REVISED VERSION: 15 November 2019

REVISED VERSION: 24 January 2020

TITLE:

Suction drain as a low carbon ground improvement technique: proof-of-concept at the laboratory scale

AUTHORS:

Michela Martini*

Alessandro Tarantino **

Andy Sloan ***

POSITION AND AFFILIATION:

* PhD, UNOPS, Health, Safety, Social and Environmental Management, København, Denmark, formerly Department of Civil and Environmental Engineering, University of Strathclyde, Glasgow, UK

** Professor, Department of Civil and Environmental Engineering, University of Strathclyde, Glasgow, UK (ORCID- ID 0000-0001-6690-748X)

*** Professor, Executive Director & Managing Director, COWI UK Ltd, Glasgow, UK.

CONTACT ADDRESS:

Alessandro Tarantino
Department of Civil and Environmental Engineering
University of Strathclyde
James Weir Building - Level 5
75 Montrose Street - Glasgow G1 1XJ, Scotland, UK
E-mail: alessandro.tarantino@strath.ac.uk

SUCTION DRAIN AS A LOW CARBON GROUND IMPROVEMENT TECHNIQUE: PROOF-OF-CONCEPT AT THE LABORATORY SCALE

Abstract

The most common soil reinforcement method used in tunnelling, such as jet grouting, fiberglass reinforcement and ground freezing, leave spoils into the ground and have high costs of implementation. On the other hand, preloading methods for soils improvement require long construction periods and limit the enhancement of the undrained shear strength to the applied surcharge load or vacuum load. This paper presents the concept of suction drain as an innovative technique for temporary stabilisation of geo structures in soft clayey soils, which overcomes the inconvenience of current soil reinforcement techniques and the limitation of the preloading. Based on suction generated into the ground by the evaporation from pre-drilled holes, the suction drain enables the enhancement of the undrained shear strength in soft clayey soils. The concept and its validation at mock-up scale level are presented in this study. The experimental investigation assessed the capacity of the suction drain to reduce the soil water content via soil water evaporation induced by forced ventilation. The mock-up scale test was then validated numerically via FEM modelling. Finally, the suction drain modelling was extended to an ideal case of tunnelling for assessing the potential impact of the suction drain on undrained shear strength and, hence, on tunnel face stability.

KEYWORDS: Clay, suction, undrained shear strength, tunnel face stability

1 Introduction

Soft clays possess very low undrained shear strength and ground improvement techniques need to be implemented prior to construction to ensure tunnel stability. The enhancement of soils shear strength is achieved by either soil reinforcement techniques or preloading.

Jet grouting and fiberglass reinforcement are the most common soil reinforcement methods used in tunnelling to ensure stability. Ground freezing is also used as temporary structural support and/or to exclude groundwater from the excavation until construction of the final lining provides permanent support. These techniques leave chemical residues and spoils into the soil or into the groundwater (liquid nitrogen and grout in the ground freezing and grouting techniques respectively), slow down construction process due to the need of cleaning up the soil after construction, and have high costs of implementation.

On the other hand, preloading methods apply the surcharge effective stress to the soft clayey soils via either the self-weight of a fill material (i.e. embankment) and/or by the vacuum pressure. Under fill surcharge, excess pore water pressures first build up from its initial (normally hydrostatic) state and then dissipate gradually. The soil undergoes consolidation and soil water content decreases, which generates higher undrained shear strength. Under vacuum pressure, the pore-water pressure in the soil reduces from its initial (normally hydrostatic) state by the same amount as the applied vacuum pressure. Again, the soil undergoes consolidation and the undrained shear strength increases. In both cases, the enhancement of undrained shear strength is limited to the applied surcharge load or vacuum load (generally smaller than 100kPa). Heavy machinery and long construction periods are also required for the fill surcharge preloading technique.

This paper explores the potential of the suction drain as an innovative technique for temporary stabilisation of geo structures in soft clayey soils. Based on suction generated into the ground by evaporation from pre-drilled holes, this technique enables the enhancement of the undrained

shear strength in soft clayey soils. No expensive equipment is required for its implementation and no spoils are left into the ground after its application (the perforated case and the inner tube for air injection are retrieved at the end of the operations). The suction drain overcomes the inconvenience of the soil reinforcement technique and the limitation of the preloading technique. The concept of the suction drain and its validation at mock-up scale level are presented in this study together with examples of its application to tunnel face stability.

2 Suction drain concept

The suction drain is conceived as a ground improvement technique to ensure temporary stability of open face tunnels and open excavations. The goal of the technique is to enhance the undrained shear strength of the soil by reducing its water content via evaporation-induced water flow.

In the proposed technique boreholes are drilled into the ground and compressed air is injected through a delivery pipe. The soil around the borehole is exposed to a continuous and constant tangential air flow at the soil interface. This generates evaporation, hence pore water pressure is depleted at the soil interface and eventually becomes negative (suction). A hydraulic head differential is generated and water is driven towards the borehole. As suction propagates from the borehole and consolidation takes place, water content in the surrounding soil reduces and undrained shear strength increases accordingly (Figure 1).

The suction drain is designed to be installed below the groundwater table. Drilling the borehole in the saturated zone will generate water flow towards the borehole, which would eventually fill up with water if there were no suction drain. However, if the evaporation rate at the borehole wall generated by the tangential airflow exceeds the influx towards the borehole, the borehole will remain dry and pore-water pressure surrounding the suction drain will be depleted from positive to negative values.

The sequence of operations related to the technology would consist in i) drilling a cased borehole to the required distance from the tunnel face by means of a dry drilling technique, ii) uncasing the borehole and installing an inner slotted case (perforated case), and iii) installing an air delivery pipe down to the end of the borehole coaxially with the borehole. Air is injected at the end of the borehole and circulates from the end to the entry of the borehole through the gap between the air delivery pipe and the inner surface of the borehole. The continuous airflow generates evaporation-induced soil water flux at the soil interface. When the water content in the surrounding of the suction drain is decreased adequately, the excavation face is advanced.

Stability is therefore insured by the suction drain-enhanced undrained shear strength, under the assumption that clayey soil deformations at the onset of failure occurs rapidly with little or no dissipation of excess pore-water pressure due to low permeability of the clayey soil (Mair & Taylor, 1997).

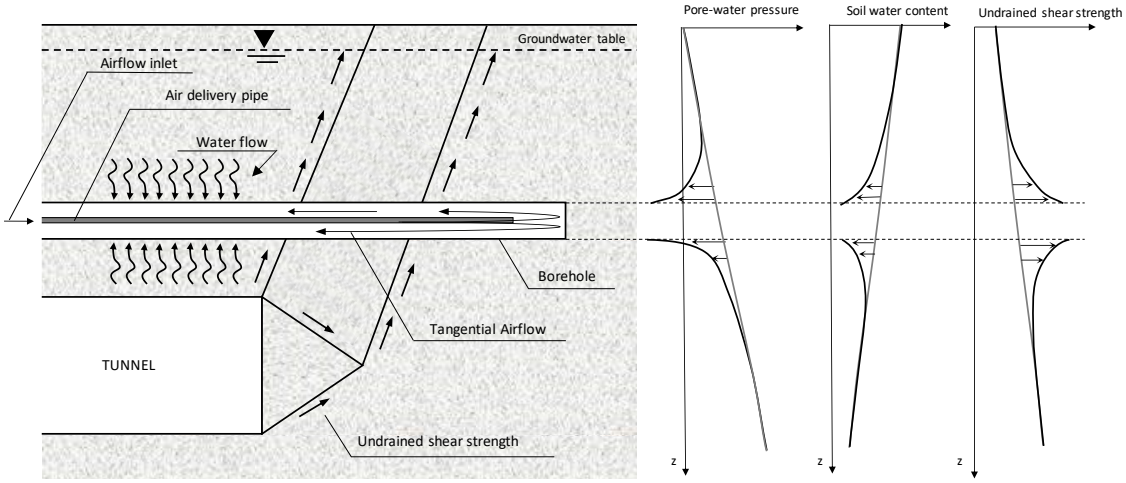

Figure 1: Concept of the suction drain (not to scale)

3 Material characterisation

3.1 Soil classification and index properties

A block sample of natural soil was taken from a working site located off Newton Farm Road in the north eastern outskirts of Newton, Cambuslang. The soil was as soft mottled orange sandy clay with bands of mottled orange sandy silt. A block sample was taken at 2.2m below ground level and was wrapped with Parafilm ® and silicon grease on site to preserve the natural soil water content. In the laboratory part of the soil from the block sample was used for soil classification and the determination of index properties. The grain size distribution, obtained via wet sieving and sedimentation, showed it to have 33% clay, 64% silt and 3% sand. The limit liquid assessed by fall cone test was LL=0.47 and the thread-rolling plastic limit was PL= 0.23. According to the plasticity chart of Casagrande, the clay is classified as inorganic clay with intermediate plasticity (PI=0.24). The soil is also classified as inactive clay with the activity A=0.73. The specific gravity was G_s= 2.66. All classification tests were carried out in accordance with BS1377:1190.

3.2 Water retention behaviour

A 50mm diameter metallic cutting ring was used to cut soil specimens from the block sample. The specimens were air-dried to target water contents then wrapped within a waterproof layer of Parafilm ® and silicon grease and stored for 24hrs to ensure water content equilibration. High-Capacity Tensiometers (HCT) (Tarantino, 2009) were used to measure the soil suction *s* in the range 0-2000kPa. Two holes were cut through the waterproof layer of the specimen and two high-capacity tensiometers were placed in contact with the surface of the specimen. A Parafilm® cover was placed around the tensiometers during the measurement to avoid water evaporation occurring from the holes. After the measurement, the sample was placed into the oven at 105˚C for 24hrs to measure the gravimetric water content.

A dew point water potentiometer (WP4C) was also used to measure suction *s* in the range 100-5000 kPa. The calibration curve of the device was verified by using sodium chloride solutions with known water potentials at 20˚C (standard deviation of error was found to be equal to ±30 kPa). Further information on the use of the WP4C can be found in Decagon Devices (2014). Specimens of approximately 1 cm^3 were cut from the 50mm diameter soil sample and were placed into the WP4C. At the end of the suction measurement, the specimens were placed into the oven at 105°C for 24hrs to measure the gravimetric water content.

Total suction (WPC4) and matric suction (HCT) versus water ratio e_w (volume of water per volume of solids) are plotted in Figure 2a. The overlap of total suction and matric suction data in the range 100 kPa-2000k Pa shows that the osmotic suction is negligible in this clayey soil.

The relationship between the soil void ratio, e and the soil water ratio, e_w was assessed independently. A 16 mm diameter and 12.5 mm high cutting ring was used to cut small specimens from the 50mm diameter soil samples after they were air-dried to target water content. The cutting ring was pushed into the sample slowly using a loading frame to prevent soil cracking. The top and bottom of the specimen were trimmed to give the specimen the same volume as the inner volume of the cutting ring, which allowed for the calculation of the void ratio. The specimen was then placed into the oven at 105°C for 24hrs to obtain the soil water content. The void ratio, e, versus water ratio, e_w, is shown in Figure 2b. Data were fitted by using the following equations:

$$e = w \cdot Gs = e_w \qquad (w > w_{AE}) \tag{1a}$$

$$e = e_{res} + \frac{e_{AE} - e_{res}}{exp[b\ (w_{AE} - w)]} \qquad (w < w_{AE}) \tag{1b}$$

where w_{AE} is the gravimetric water content at air entry, G_s is the specific gravity of the soil, e_{res} is the residual void ratio, e_{AE} is the void ratio at air entry, and b is a fitting parameter. It is

possible to see that upon drying, the void ratio decreases to $e = 0.53$ in the saturated range then remains constant when the soil desaturates.

The drying curve in terms of degree of saturation, S_r versus soil suction, s, is shown in Figure 2c. For each data point of known water ratio, e_w, and soil suction, s, the degree of saturation S_r was calculated as per the ratio of water ratio to void ratio ($S_r = e_w/e$) with void ratio e obtained from Equation (1). Experimental data of the degree of saturation, S_r versus soil suction, s, were fitted with the van Genuchten's function (van Genuchten, 1980):

$$S_r = \left(\frac{1}{1 + (\alpha s)^n}\right)^m \tag{2}$$

where α, n and m are fitting parameters.

The relationship of void ratio, e versus soil suction, s is shown in Figure 2d. Experimental data were fitted by using the following equations:

$$e = e_k - k \cdot ln(s) \qquad (s < s_p) \tag{3a}$$

$$e = N - \lambda \cdot ln(s) \qquad (s_p < s < s_{AE}) \tag{3b}$$

$$e = e_{res} + \frac{e_{AE} - e_{res}}{exp(a\,(s - s_{AE}))} \qquad (s > s_{AE}) \tag{3c}$$

where s_p is the suction associated with the preconsolidation effective stress, s_{AE} is the suction at air entry, e_k, k, N, λ and a are fitting parameters. From Figure 2d it is possible to see that the soil is over consolidated for soil suction lower than s_p=177kPa, normally consolidated at suctions between s_p=177kPa and s_{AE}=420kPa, and it desaturates at soil suction greater than s_{AE}=420kPa.

Ultimately, the water retention behaviour in terms of volumetric water content, θ, was defined by the product of the porosity, n and the degree of saturation, S_r ($\theta = n \cdot S_r$). The values of the parameters used to characterise the water retention behaviour of the soil are given in Table 1.

Table 1: Parameters for the water retention behaviour

w_{AE} [-]	e_{res} [-]	e_{AE} [-]	b [-]	α [kPa]$^{-1}$	n [-]	m [-]
0.205	0.531	0.545	186.593	0.00199	9.748	0.0279
s_p [kPa]	s_{AE} [kPa]	e_k [-]	k [-]	N [-]	λ [-]	a [kPa]$^{-1}$
177.417	419.679	0.796	0.034	1.065	0.086	0.0144

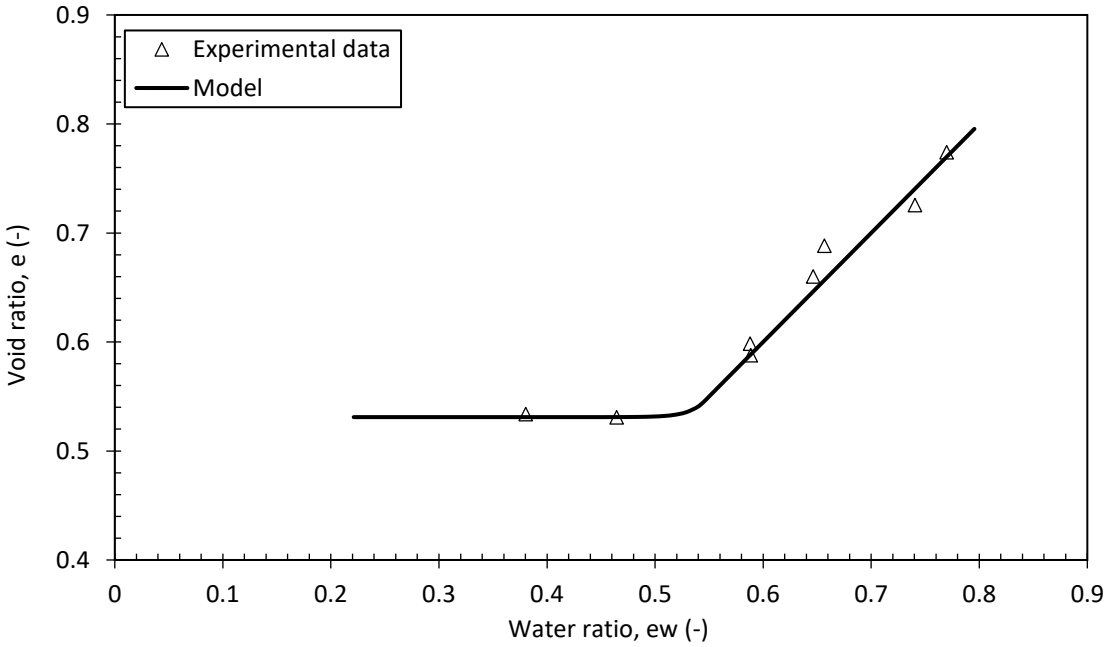

(a)

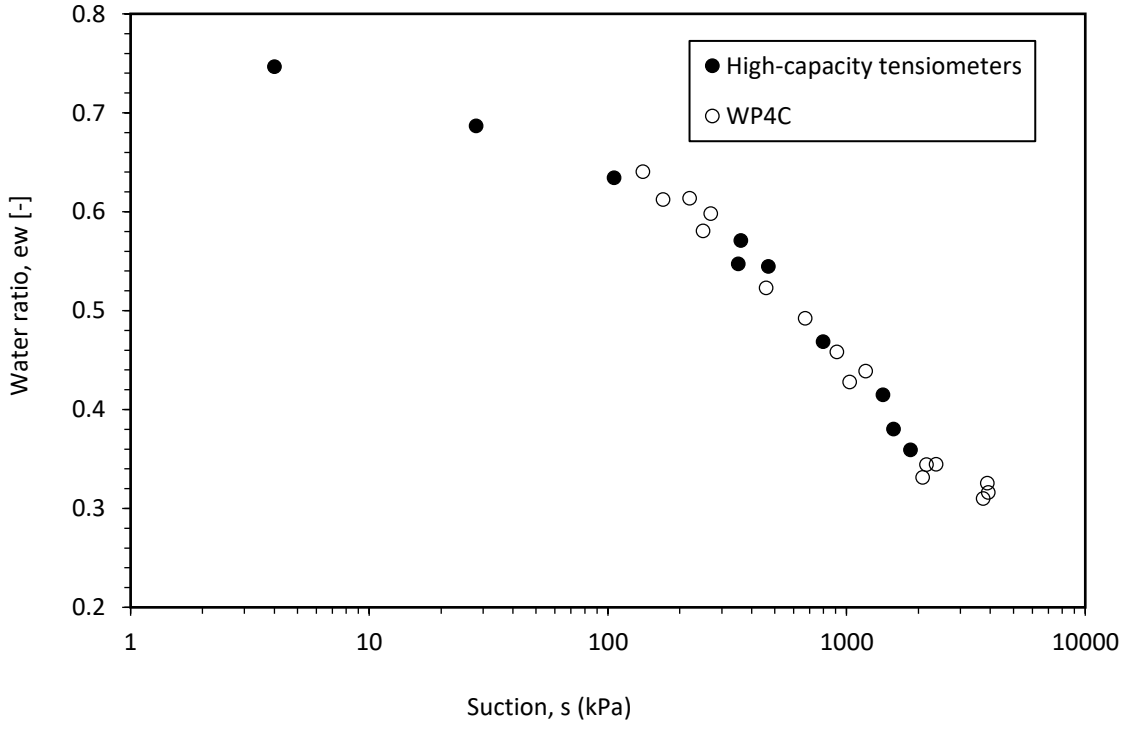

(b)

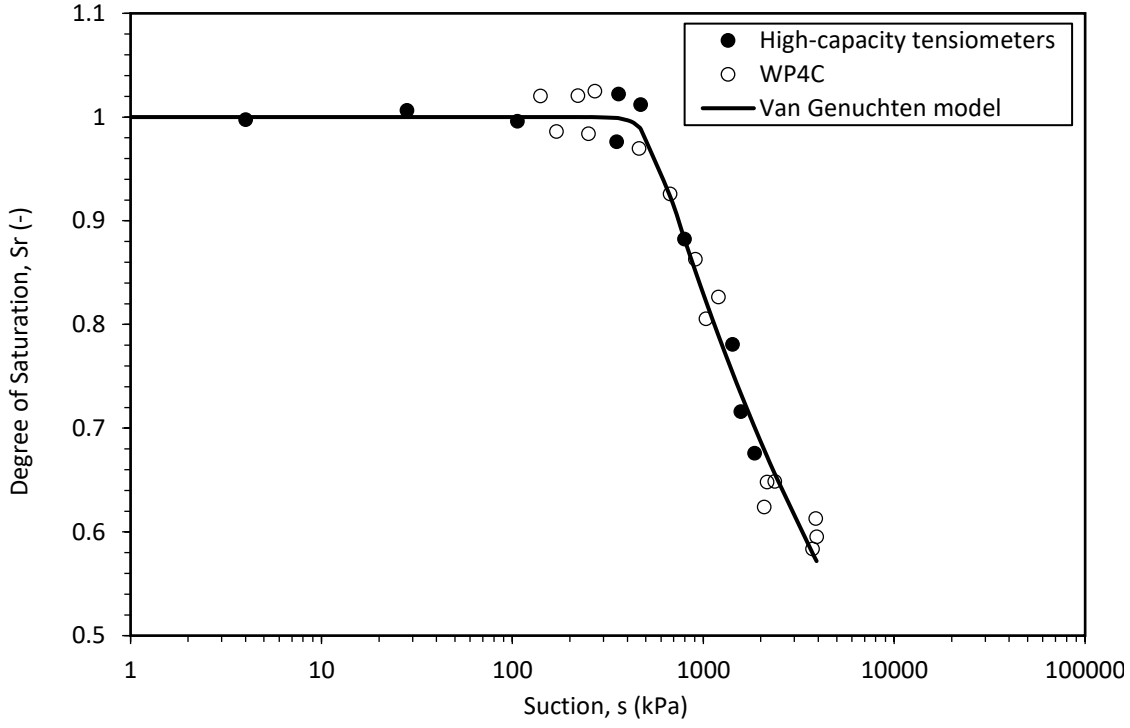

(c)

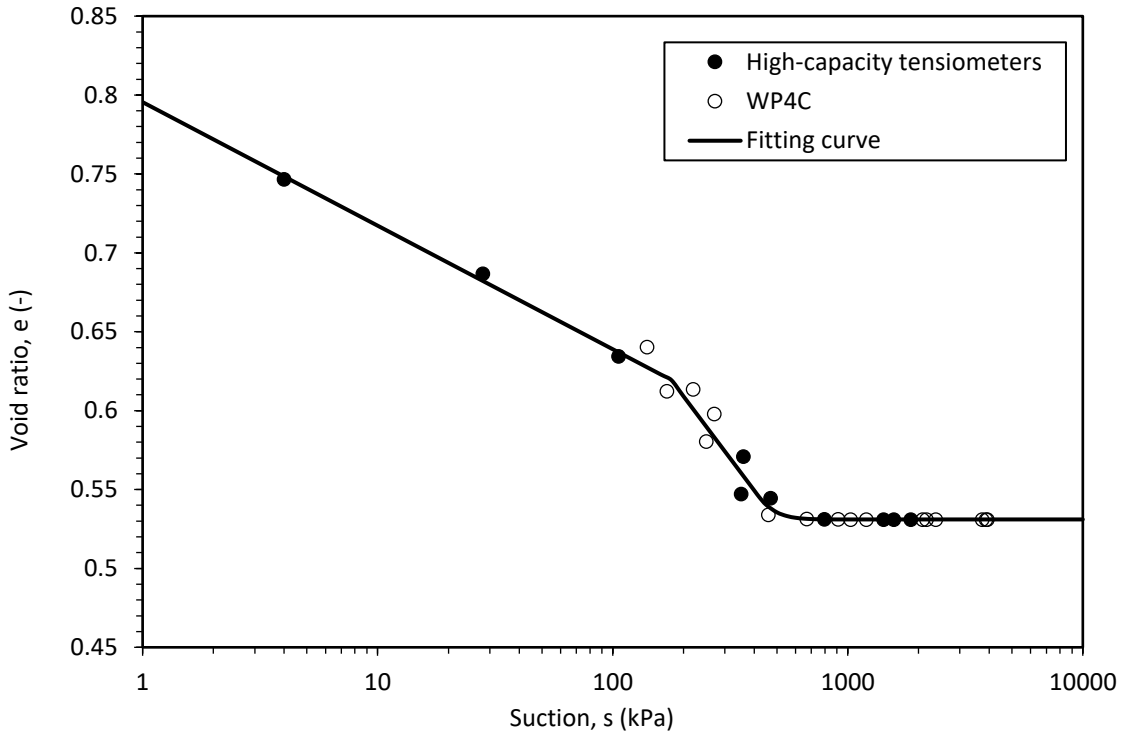

(d)

Figure 2: Water retention behaviour of the soil material used for the mock-up scale test. (a) Void ratio versus water ratio. (b) Water ratio versus suction. (c) Degree of saturation versus suction. (d) Void ratio versus suction.

3.3 Hydraulic conductivity behaviour

The Kozeny-Carman equation suggested by Tarantino et al. (2010) was used to model the hydraulic conductivity:

$$k = k_{sat}\left(\frac{e}{e_0}\right)^3\left(\frac{1+e_0}{1+e}\right)S_r^3 \tag{4}$$

where k_{sat} is the saturated hydraulic conductivity associated with the reference soil void ratio e_0, e is the void ratio, and S_r is the degree of saturation. The void ratio e and the degree of saturation S_r were obtained from Equation (3) and Equation (2) respectively. The hydraulic conductivity curve is shown in Figure 3.

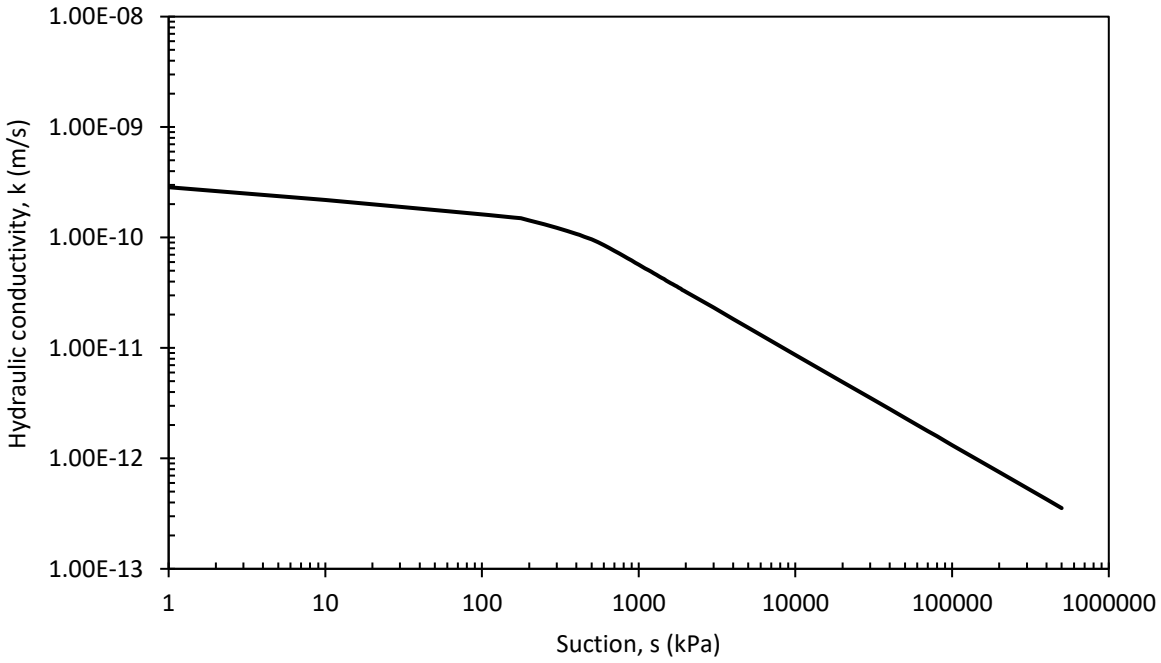

Figure 3: Hydraulic conductivity model of the soil material used for the mock-up scale test

The saturated hydraulic conductivity k_{sat} was assessed experimentally via a constant head hydraulic conductivity test carried out in a modified oedemeter cell. A 75mm diameter and 20mm high soil specimen was cut from the block sample by using the oedometer cutting ring. The specimen was placed into the oedometer, covered with water, and loaded in steps to a maximum vertical stress of $\sigma_v = 1428$ kPa. The oedometer cell was connected to a reservoir of water located at *H*=1.062m above the water level of the oedometer. At the end of the primary

consolidation of selected loading step, the valve connecting the base of the oedometer to the reservoir was opened and the water was allowed to flow upwards through the specimen. The amount of water passing through the specimen was measured by the balance underneath the water reservoir, accounting for the loss of mass of water due to the evaporation from the water reservoir. Three hydraulic conductivity tests were carried out at the vertical stresses of $\sigma_{v1} = 90\text{kPa}$, $\sigma_{v2} = 179\text{kPa}$ and $\sigma_{v3} = 357\text{kPa}$, associated with void ratios of $e_1 = 0.70$, $e_2 = 0.67$, and $e_3 = 0.62$ respectively (Figure 4). The hydraulic conductivity k_{sat} was calculated by means of Darcy's law.

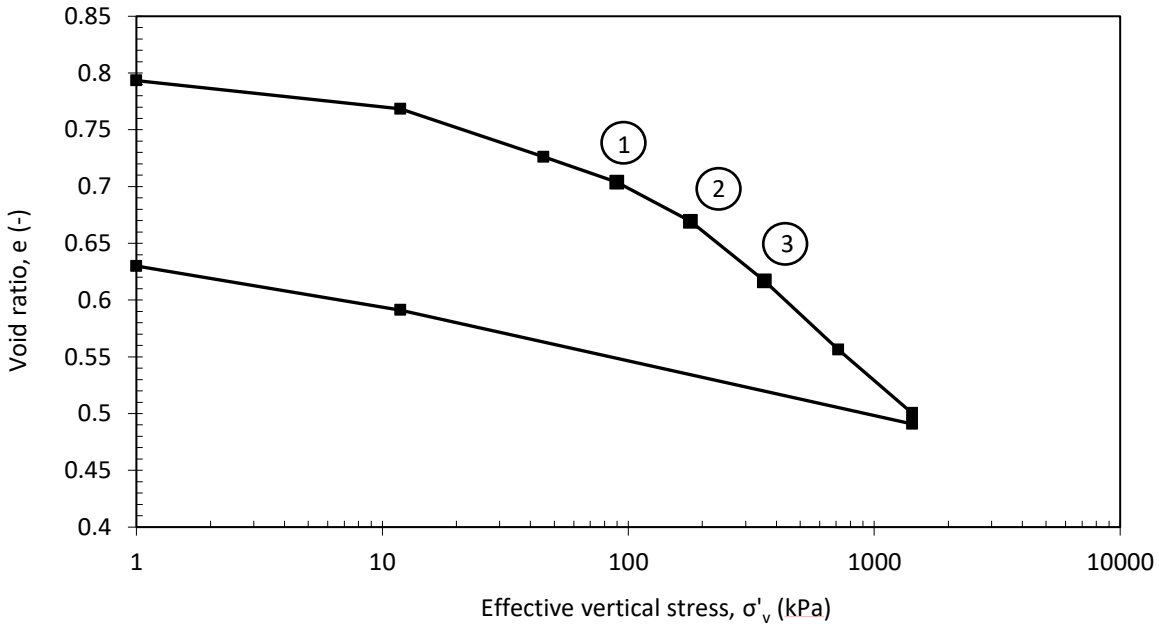

Figure 4: Compressibility curve of the soil and indication of the loading steps where the permeability tests were carried out

Direct measurements of k_{sat} versus $e^3/(1+e)$ are shown in comparison with the values of k_{sat} derived from the Terzaghi's consolidation theory in Figure 5. The experimental k_{sat} and k_{sat} from the consolidation theory are within the same order of magnitude and vary linearly with $e^3/(1+e)$. The linear relationship is supported by the Kozeny-Carman model (Mitchell & Soga, 2005) and was used as a check of the quality of the hydraulic conductivity tests (Chapuis & Aubertin, 2003). The offset between the two series of data might be explained by

the fact that the Terzaghi's theory of consolidation assumes the soil to be linearly elastic and k_{sat} to remain constant throughout the consolidation process.

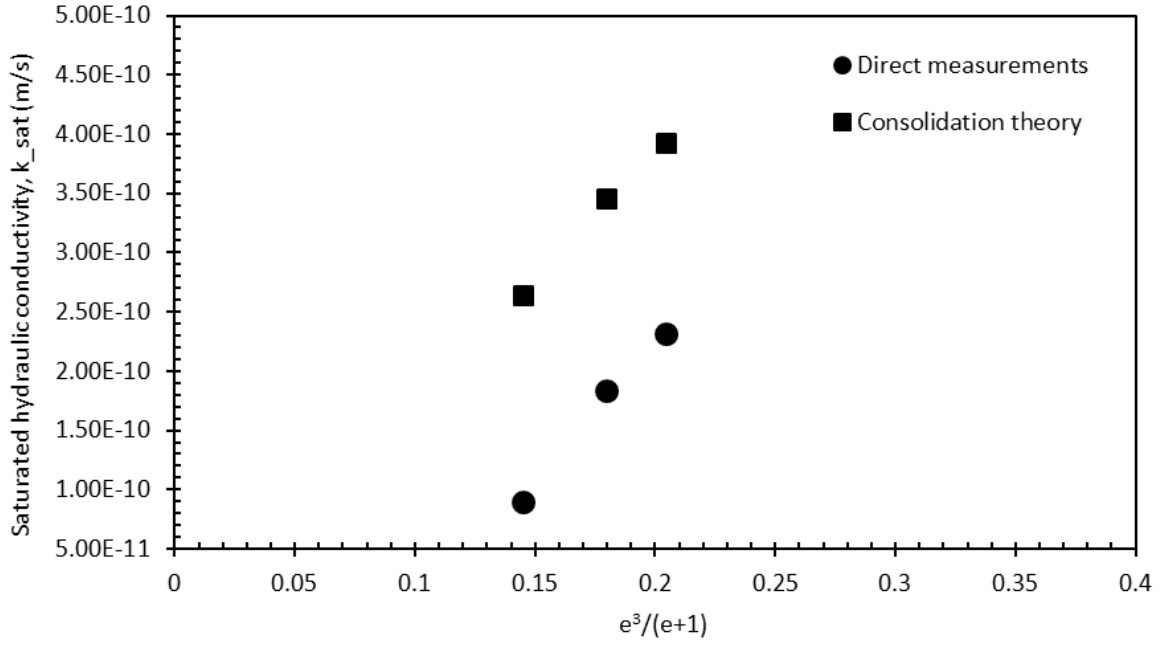

Figure 5: Saturated hydraulic conductivity of the soil material used for the mock-up scale test

4 Boundary condition characterisation

An independent study was carried out to quantify the water evaporation from the inner surfaces of the suction drain that are exposed to a tangential airflow of a known air velocity and relative humidity in a confined space (Martini & Tarantino, 2020). To this end, the apparatus shown in Figure 6 was designed in the laboratory with an upper air channel of dimensions similar to the confined space in the suction drain and a bottom container that simulates the evaporating surface of the suction drain. Compressed air was injected through the upper air channel so that airflow circulated tangentially to the wet surface of the water-filled container. Tests were carried out by considering different air velocities and relative humidities (*RH*) of the airflow at the inlet. The relative humidity at the inlet RH_{inlet} and the velocity of the airflow were measured via the RH/T sensor (Sensirion Kit EK-H5 sensors SHT21) and the anemometer (OMEGA

FMA1006R-V2-S) installed at the inlet of the upper air channel respectively. The average water evaporation rate was measured over time by the two balances installed at the bottom of the water-filled container.

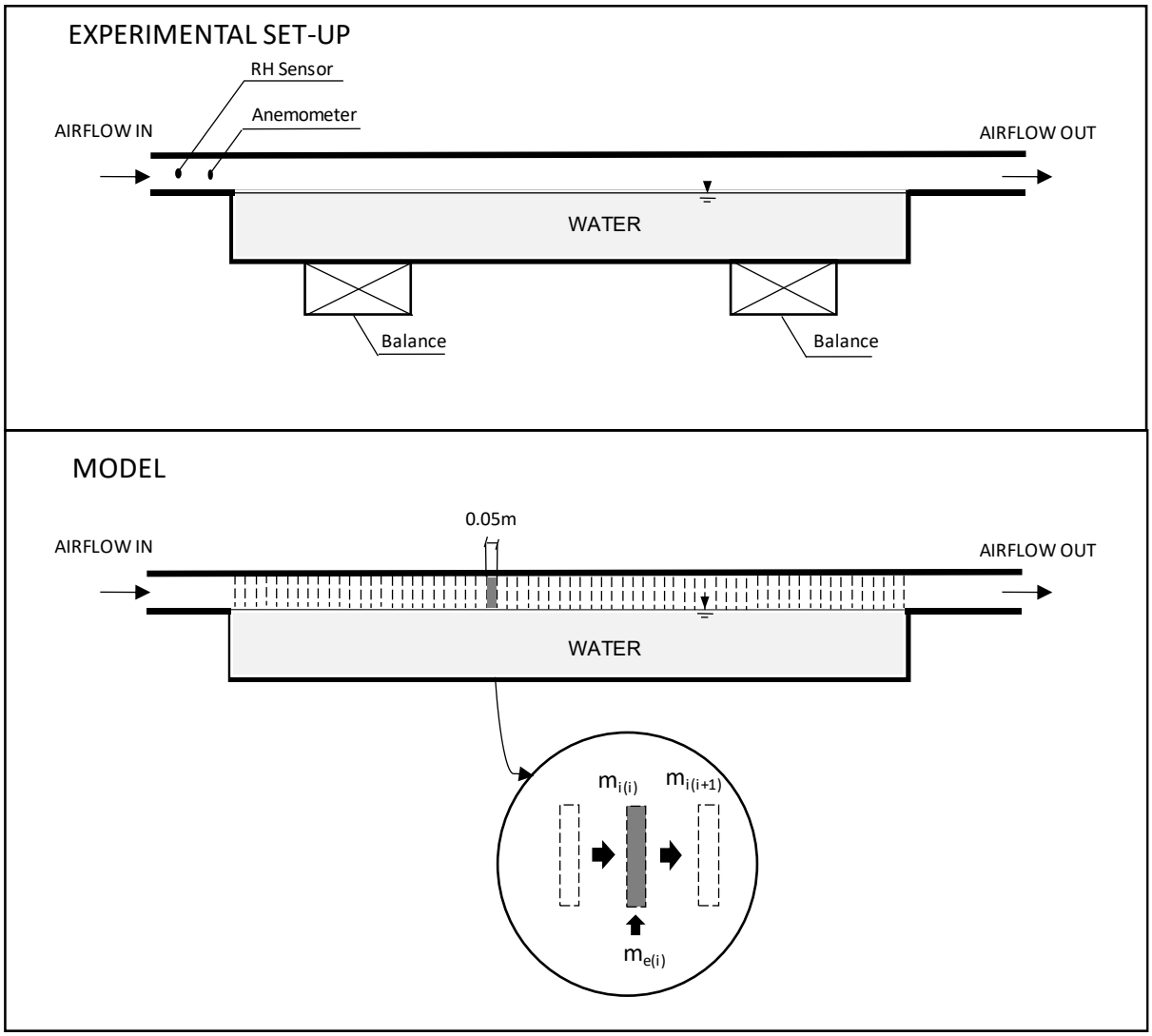

Figure 6: Experimental set-up and model for characterising the boundary condition in terms of water flow per unit area and unit time, q (m/s)

A model was formulated to quantify the water evaporation rate for any length of the wet surface. The upper air channel above the evaporating surface was divided into 0.05m wide elements as shown in Figure 6. In each element the water mass balance was calculated as follows:

$$m_{in(i)} + m_{ev(i)} = m_{out(i)} = m_{in(i+1)} \quad (5)$$

where $m_{in(i)}$ is the mass of water vapour carried by the airflow at the inlet of each element *i*, $m_{ev(i)}$ is the mass of water that evaporates from the water surface at the bottom of each element *i* in turn function of the water evaporation rate $q_{(i)}$, $m_{out(i)}$ is the mass of water vapour carried by the airflow at the outlet of each element *I*, and $m_{in(i+1)}$ is the mass of water vapour carried by the airflow at the inlet of the element *i+1*. The water evaporation rate $q_{(i)}$ at the bottom of each element *i* was calculated by using of the following equation:

$$\mathrm{q_{(i),model}} = \alpha[\mathrm{v_{air}}(z)] \cdot \mathrm{p_{vo}} \cdot (1 - \mathrm{RH_{in(i)}}) \tag{6}$$

where $\alpha[v_{air}(z)]$ is the vapour transfer coefficient (depending on air velocity), p_{vo} is the equilibrium vapour pressure at saturation (depending on the temperature of the airflow), and $RH_{in(i)}$ is the relative humidity of the airflow at the inlet of the element *i*. The vapour transfer coefficient α is the sole parameter of the model and was calibrated by imposing that:

$$\mathrm{q_{model}} = \frac{\sum_1^{\mathrm{n}} \mathrm{q_{(i),model}} \cdot \Delta l_i}{\sum_1^{\mathrm{n}} \Delta l_i} = \mathrm{q_{experimental}} \tag{7}$$

where q_{model} is the simulated average evaporation rate, $q_{(i),model}$ is the simulated local evaporation rate associated with the *i-th* element, Δl_i is the width of the *i-th* element, and $q_{experimental}$ is the average evaporation rate measured via the balances in the tests where the *RH* of the airflow at the inlet was equal to RH_{inlet}=0 and air velocity varied from v_{air}=1m/s to v_{air}=4m/s. The model was then validated for tests with airflow at different inlet relative humidity.

It is worth highlighting that the vapour transfer coefficient α was detected under steady-state air-flow conditions and that the hypothesis of steady state air-flow condition was assumed to be valid in water-flow transient process. The vapour transfer coefficient α inferred from the test with airflow at v_{air}=4m/s on water surface was found to be the same as the coefficient α inferred from the test on saturated soil exposed to the airflow at the same air velocity.

The values of the vapour transfer coefficient α against the air velocity are shown in Figure 7. These values of α allowed estimating the boundary conditions in terms of water evaporation rate (Equation (6)) for the suction drain model.

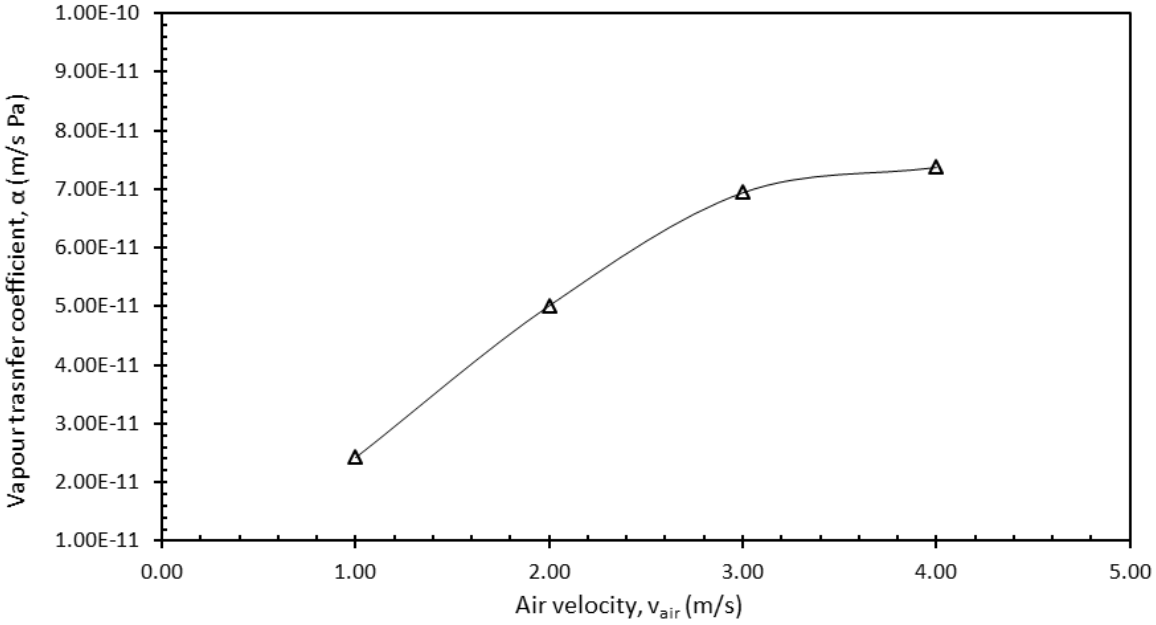

Figure 7: Experimental vapour transfer coefficient, α versus the velocity of the airflow, v_{air}

5 Suction drain mock-up scale test

5.1 Set-up

A mock-up scale test was designed to provide a proof-of-concept of the suction drain technique at the laboratory scale (Figure 8). A cylindrical specimen 300mm diameter and 150mm high was cut from the block sample taken from the field. The external surface of the specimen was made waterproof by using a layer of silicon grease and Parafilm® to prevent water evaporation. A central borehole 70mm diameter was drilled through the specimen. A metal air delivery tube 700mm long, 15mm OD was placed centrally into the borehole and was kept suspended at 25mm distance from the bottom of the soil sample to allow the airflow to circulate from the bottom to the top through the gap between the delivery tube and the borehole. A 500mm high

and 80mm diameter plastic case was placed at the entry of the borehole to isolate the air flow from the environment.

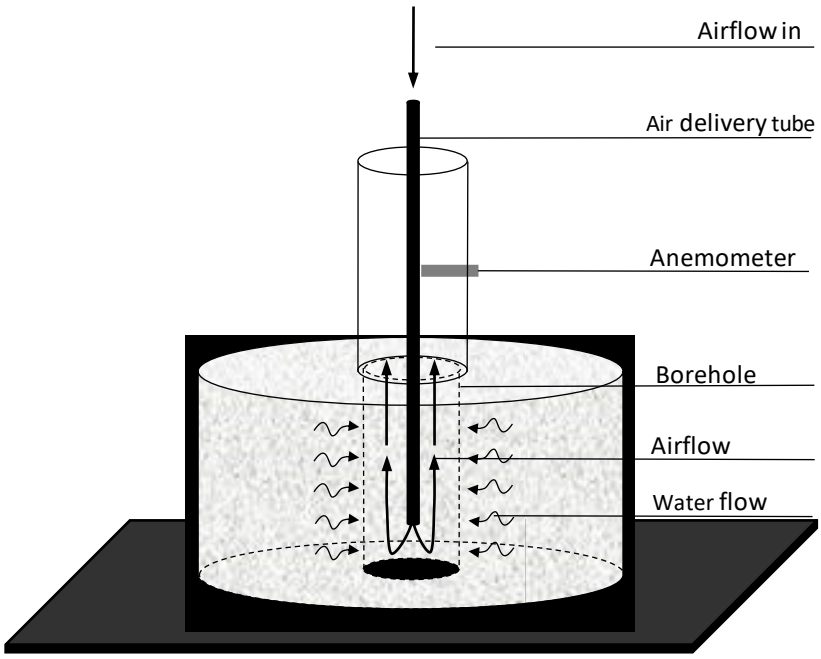

Figure 8: Schematic layout of the mock-up scale test

Air velocity and temperature of the airflow were measured via an anemometer placed perpendicular to the airflow at the inlet of the air delivery tube. The anemometer is detailed in Appendix I.

5.2 Experimental Procedure

A continuous airflow was injected inside the borehole through the inner delivery tube 24/7 for 6 days at the air velocity v_{air}=2m/s and air temperature T=20°C.

The variation of the soil water content was monitored over time at different distances from the central borehole. Four 150mm long and 15mm diameter core samples were sampled every day to measure the water content according to the scheme shown in Figure 9. Two samples were taken at 35mm from the central borehole (solid line) and two samples were taken at 70mm from the central borehole (broken line). Each 50mm-long sample was divided in three parts (top, middle, and bottom) and each part was placed in the oven at 105˚C for 24 hours to measure

the gravimetric water content. After each sampling, the hole was sealed with silicon grease and Parafilm ® in order to avoid extra evaporation occurring from the sampling hole. Since the cylindrical hollow specimen was assumed to have homogeneous initial water content and the evaporation-induced soil water flux was asymmetric, samples were taken from a different portion of the hollow specimen each day as shown in Figure 9. By using this scheme, the sampling of previous days did not interfere with the sampling of following days.

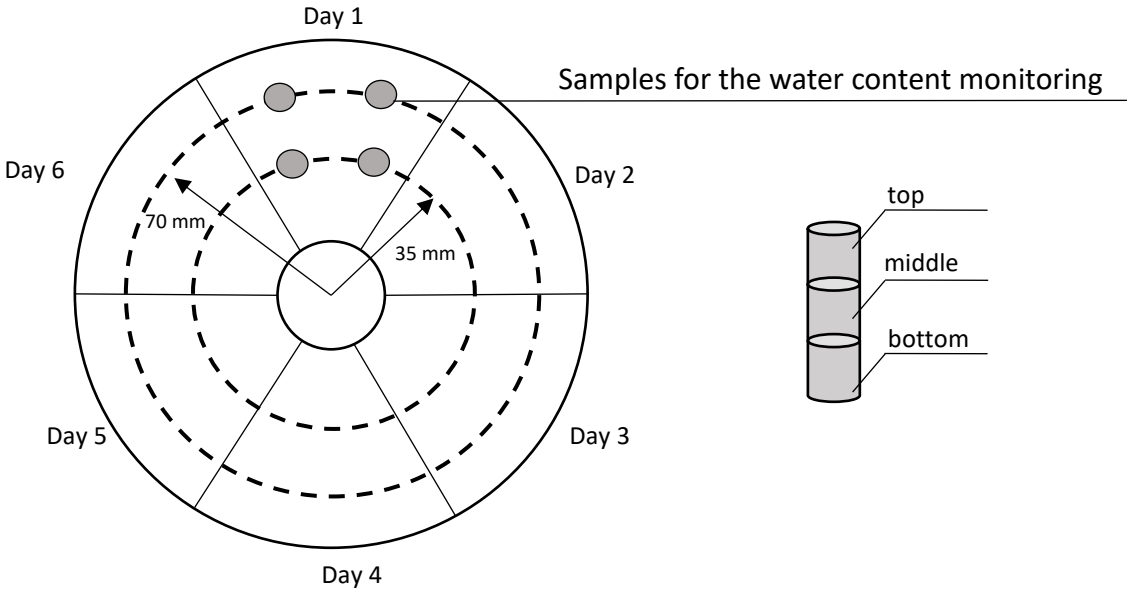

Figure 9: Schematic layout of the soil sampling in the mock-up scale test for monitoring the soil water content

5.3 Results

The results from the mock-up test are presented in Figure 10. The gravimetric water content, *w* of each soil sample at 35mm and at 70mm from the central borehole is plotted versus the time, *t*.

The soil water content decreased over time from the initial value w=0.29 to the final values w=0.16 and w=0.11 for samples at 70mm and 35mm distance from the borehole respectively. In Figure 10, it can be observed that soil water content decreased at a slower rate when the soil desaturated (w<0.18). As expected, the soil water content recorded at 35mm decreased at a faster rate than the soil water content at 70mm (soil samples at 35mm distance were closer to

the central borehole where evaporation occurred). The average water content of the soil samples at 35mm distance was about 0.03-0.05 smaller than the average water content of the soil samples at 70mm distance over the duration of the experiment.

It can also be observed that the soil water content of the top, middle and bottom parts of each soil sample differed by 0.02-0.04 without a consistent pattern. A possible explanation is the presence of sand lenses in the hollow specimen, which possibly led to some scattering in the soil water content.

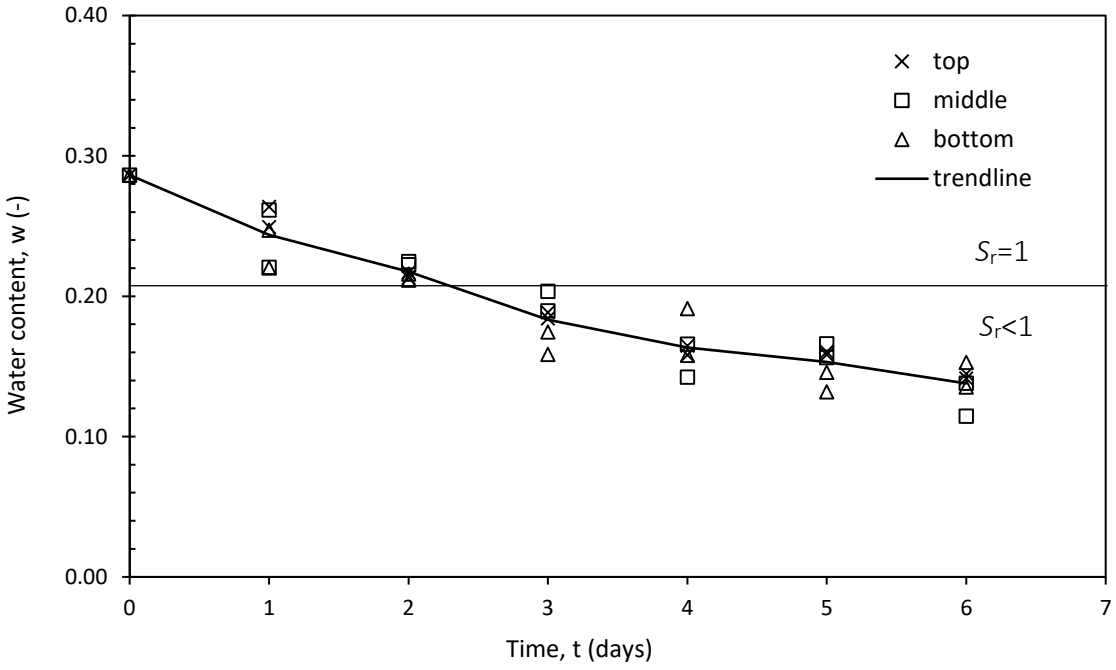

(a)

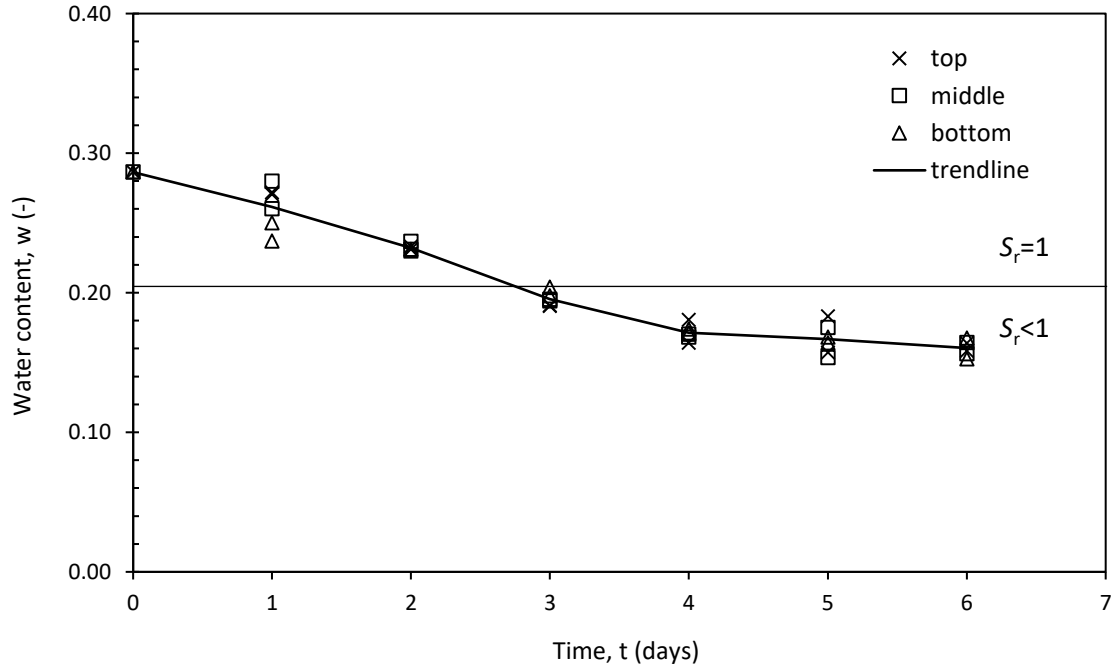

(b)

Figure 10: Experimental soil water content in the mock-up scale test. (a) at 35mm from the central borehole; (b) at 70mm from the central borehole

6 Water flow modelling of the suction drain mock-up test

This section aims to simulate the evaporation-induced water flow that was generated into the block of natural soil during the mock-up test. An axisymmetric finite element analysis was conducted to simulate the water content of the soil around the borehole in the mock-up test.

6.1 Hydraulic model

The hydraulic-mechanical model that simulates water flow generated by tangential airflow in the suction drain was derived from Tarantino et al. (2010). Water evaporation at the borehole surface generates a gradient in pore-water pressure which, in turn, generates a water flow towards the inner surface of the borehole. In an initially saturated soil, changes in pore-water pressure cause mechanical deformation of the clay skeleton that affects its water storage capacity. Hence, the evaporation-induced water flow is a hydro mechanical coupled process, i.e. water mass balance and momentum balance equations are in principle required to be solved simultaneously.

The water mass balance can be written as follows:

$$div(\vec{v}) = \frac{\partial \theta}{\partial t} \tag{8}$$

where $\vec{v}$ is the flow velocity, θ is the volumetric water content (volume of water per total volume), and t is the time. In Equation (8), the flow velocity is given by the Darcy-Buckingam law (Fredlund & Rahardjo, 1993, Lu & Likos, 2004):

$$\vec{v} = -k\,(e, Sr)\; grad\left(\frac{u_w}{\gamma_w} + z\right) \tag{9}$$

where u_w is the pore-water pressure, z is the vertical coordinate increasing upward, γ_w is the specific weight of water, and k is the hydraulic conductivity, which depends on void ratio e

and degree of saturation S_r (Mitchell & Soga, 2005). Equation (9) neglects diffusive and advective transport of water vapour and this assumption is corroborated by numerical simulation of isothermal drying in low-permeability materials (Baroghel-Bouny, et al., 2001; Coussy, 2004). The volumetric water content can be expressed as a function of S_r and e as follows:

$$\theta = \frac{e(p, u_w)}{1 + e(\sigma_{ij}, u_w)} \cdot Sr(u_w) \tag{10}$$

where the void ratio e and, hence, the volumetric water content θ, depend on the pore water pressure and on the total isotropic stress p. It follows that the second term of Equation (8) becomes:

$$\frac{\partial \theta}{\partial t} = \frac{\partial \theta}{\partial \sigma} \cdot \frac{\partial p}{\partial t} + \frac{\partial \theta}{\partial u_w} \cdot \frac{\partial u_w}{\partial t} \tag{11}$$

Since the total radial stress at the boundaries of the mock-up scale test is σ_r=0kPa, the variation of the total stress $\partial p/\partial$t can be assumed to be negligible in comparison to the variation of the pore water pressure $\partial u_w/\partial$t. This point is discussed in Appendix II for the case of a saturated material. An analytical solution for the stress state in the thick walled hollow cylinder was derived analytically and it is shown that $\partial p/\partial t$, although different from zero, is relatively small compared to that $\partial u_w/\partial t$ and can be neglected as a first approximation in Equation (11).

By assuming $\partial p/\partial t$=0, the volumetric water content only depends on u_w (Equation (10)) and Equation (8) simplifies to a single-variable partial differential equation as follows:

$$\frac{\partial}{\partial x}\left[k \cdot \frac{\partial}{\partial x}\left(\frac{u_w}{\gamma_w}\right)\right] = \frac{\partial \theta(u_w)}{\partial u_w}\frac{\partial u_w}{\partial t} \tag{12}$$

with the following boundary conditions:

$$q(l, t) = \alpha(v_{air}) \cdot p_{v0}(T_{air}) \cdot (RH_{soil} - RH_{air}) \tag{13}$$

$$q\,(L, t) = 0 \tag{14}$$

and initial condition:

$$u_w(x,0) = u_{w0} \tag{15}$$

where *x*=l coincides with the inner surface of the borehole and *x*=L coincides with the external surface of the block of soil. The term q is the water evaporation rate, α is the vapour transfer coefficient that is a function of the air velocity, p_{v0} is the saturated vapour pressure that is a function of the temperature of the airflow, RH_{soil} is the relative humidity at the inner surface of the borehole, and RH_{air} is the relative humidity of the airflow. The vapour transfer coefficient $\alpha(v_{air})$ was determined experimentally as illustrated in Section 4. The relative humidity at the clay surface RH_{soil} is related to the soil suction by the psychrometric law:

$$RH_{soil} = exp\left[\frac{v_w s}{RT}\right] \tag{16}$$

where v_w is the molar volume of liquid water, s is the soil suction, R is the universal constant of gas, and T is the absolute temperature. Equation (12) together with the boundary conditions and the initial condition given by Equations (13), (14) and (15) was solved via finite element analysis.

Non-linear hydraulic constitutive functions were considered. The hydraulic conductivity k was modelled using the Kozeny-Carman model (Equation (4)) and illustrated in Figure 3 for the material characterised in Section 3. The function $\theta = \theta(u_w)$ was derived from the void ratio e and the degree of saturation S_r as follows:

$$\theta = \frac{e(u_w)}{1 + e(u_w)}\, Sr\,(u_w) \tag{17}$$

where the void ratio $e(u_w)$ is defined by Equation (3) and illustrated in Figure 2d for the material characterised in Section 3 and the degree of saturation $Sr\,(u_w)$ is defined by Equation (2) and illustrated in Figure 2c for the material characterised in Section 3.

6.2 Numerical analysis and results

The finite element mesh is shown in Figure 11 and represents a radiant section of the mock-up test with the vertical axis of the model coinciding with the axis of symmetry. The initial condition was specified in terms of pore-water pressure that enables the water content of the soil to be equal to the soil water content measured experimentally before the test (w=0.29). Boundary conditions were specified in terms of water flow. This was set equal to q=0 m/s at the top, bottom and outer surface of the model, and was given by Equation (13) at the inner surface of the model. The vapour transfer coefficient α was derived from Figure 7 as a function of the air velocity ($\alpha = 5.02 \text{ x } 10^{-11}\text{m/s}$ for $\text{v}_{\text{air}} = 2\text{m}$), the saturated vapour pressure was set equal to $p_{v0}(20°\text{C}) = 2.34$ kPa, and the average relative humidity of the airflow along the borehole was set equal to $RH_{air} = 0$. The value RH_{air} was consistent with the relative humidity of the airflow from the compressed air system measured via the RH/T sensor placed at the outlet of the air delivery tube. The relatively short length of 150mm of the borehole allowed assuming that the relative humidity of the airflow remains constant along the borehole. This assumption is based on previous experimental observation (Martini & Tarantino, 2020). Parameters used for the psychrometric law are presented in Table 2.

Table 2: Parameters for Psychrometric Law

ν_w [m^3/mol]	R [J (K mol)$^{-1}$]	T [K]	p_{v0} at T= 20·C [kPa]
18 x 10^{-6}	8.314	293	2.34

The water retention curve and the hydraulic conductivity curve measured experimentally (Figure 2 and Figure 3) were used to model the soil in the numerical analysis. The analysis was run for 6 days and adaptive time steps were used to optimise the convergence.

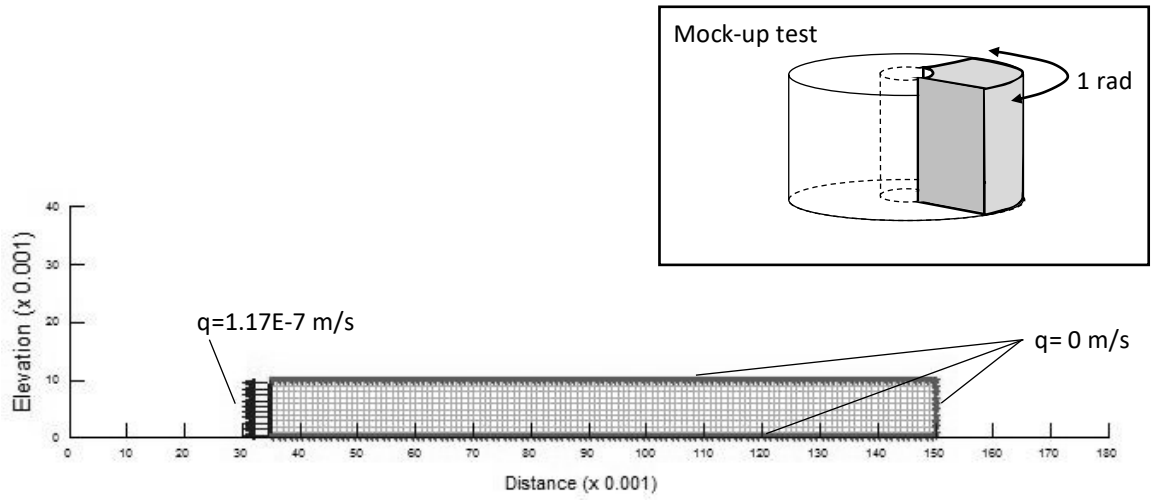

Figure 11: Numerical modelling for the validation of the mock-up scale test (axisymmetric conditions)

Simulated soil water content at 35mm and 70mm from the central borehole are compared with the average experimental soil water content measured at the same distances in the mock-up test over time in Figure 12. It can be observed that the numerical simulation is in fair agreement with the experimental data. This indicates that the suction drain numerical model presented in this section represents adequately the evaporation-induced water flow generated in the clay sample.

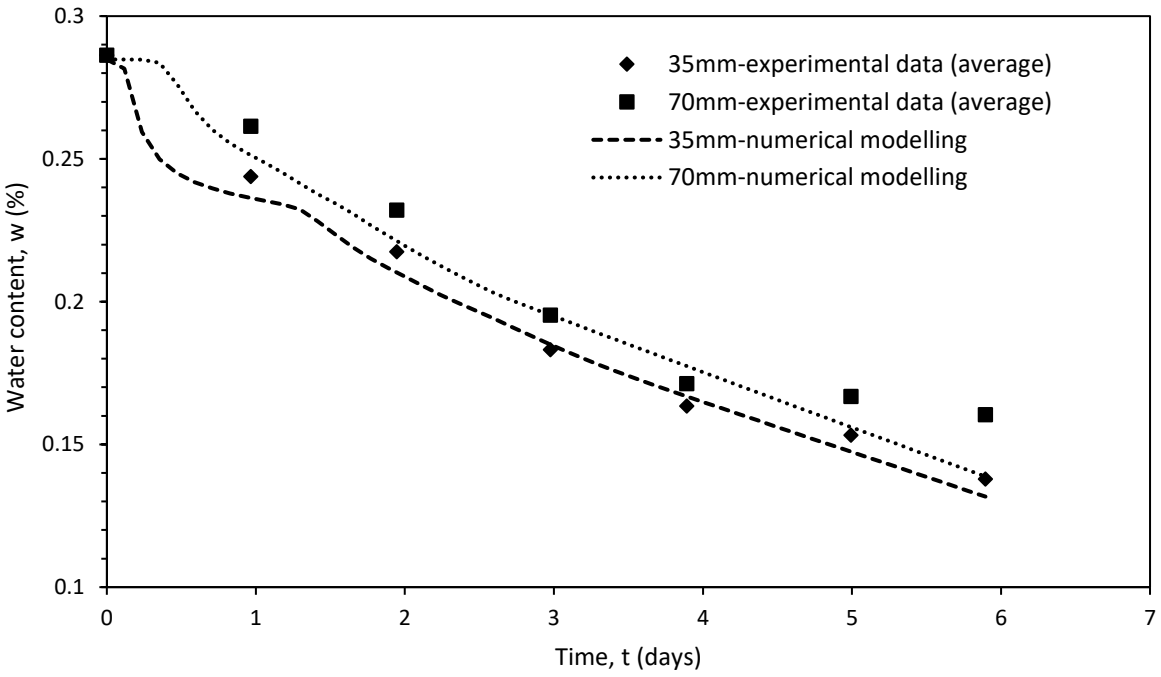

Figure 12: Comparison between the experimental and the numerical soil water content, w versus time, t

7 Effectiveness of suction drain in stabilising tunnel face

This section explores the beneficial effects of the suction drain in stabilising tunnel face. The suction drain reduces the water content of the surrounding soil and, hence, increases its undrained shear strength. The undrained shear strength of the soil provides the soil resistance to collapse to the tunnel. When the tunnel is excavated, the overburden applies an inward pressure to the front of the tunnel and the undrained shear strength of the soil mobilised along the failure mechanism provides the soil resistance to the collapse (Leca & New, 2007). The stability of the front of a tunnel is expressed by the stability factor N that is defined by the following Equation (Broms & Bennermark, 1967):

$$N = \frac{\gamma \cdot \left(C + \frac{D}{2}\right)}{c_u} \tag{18}$$

where γ is bulk unit weight of the soil, C is the depth of cover, D is the tunnel diameter, and c_u is the undrained shear strength of the overburden. An increase of the undrained shear strength of the overburden results in increased stability of the tunnel face and, hence, in a decrease of the stability factor *N*.

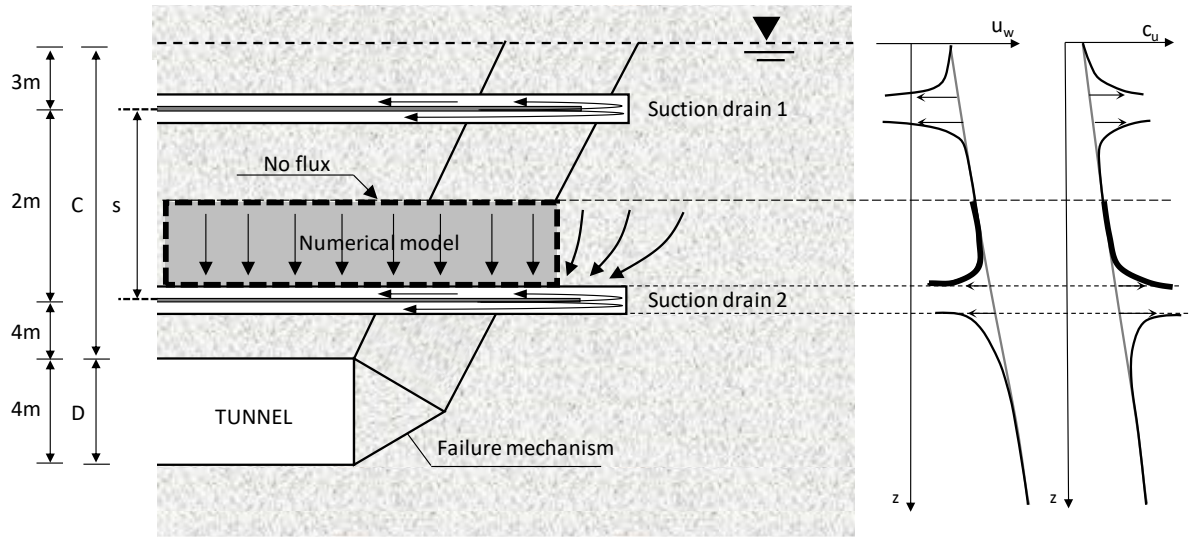

Figure 13: Numerical model of the suction drain in tunnelling (drawing not to scale)

The design of the suction drains would include drilling the boreholes in an umbrella arch configuration above the crown of the tunnel. Boreholes are drilled from the crown of the excavation face of the tunnel or from a higher vertical wall prior the excavation of the tunnel (i.e. shaft, bigger diameter tunnel normal to the tunnel in excavation). For the sake of this exercise, a simplified configuration of the excavation of the suction drains is considered. Two rows of suction drains are excavated with a spacing of 2m in the overburden of the tunnel with the excavation axis parallel to the axis of the tunnel. The tunnel is 4m diameter and is excavated with its axis at 11m below ground level as illustrated in Figure 13.

Figure 13 also presents the numerical model. The three-dimensional (3D) problem of the evaporation-induced water flow at the inner surface of the borehole is studied as a two-dimensional (2D) problem. Suction drains are modelled as planes, having an infinitive depth in the dimension out of the page. Under these conditions, the flow net is expected to be 2D at the entry and end of the borehole whereas it is essentially 1D along the length of the borehole far-off from the ends. The flow is symmetric between two suction drains and the line 'No Flux' indicates the mid-plane between two drains. In this exercise, only a column of soil that extends from the surface of the lower suction drain to the suction drain mid-plane (from 4m to 5m as illustrated in Figure 13) was modelled to investigate the evaporation-induced water flow between two suction drains (Figure 14).

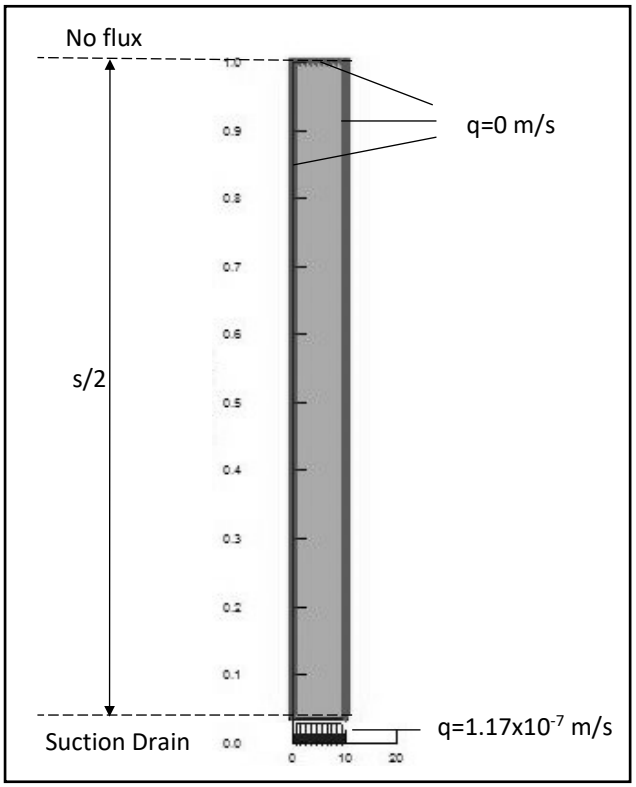

Figure 14: 1D finite element mesh and boundary conditions of the numerical model

Initial and boundary conditions of the model were defined in terms of pore water pressure and water evaporation rate, respectively. The initial pore water pressure was assumed to be hydrostatic and equal to 50kPa at the base of the column according to Figure 13. The evaporative water flux at the bottom surface of the column, which coincides with the inner surface of the borehole of the suction drain, was defined via Equation (13) with the vapour transfer coefficient equal to the one derived for the mock-up scale test ($q = 1.17\text{x}10^{-7}\text{m/s}$ for RH_{soil}=100%).

The water retention behaviour of the soil in the unsaturated range was described by the water retention curve versus suction used for the mock-up test with the following changes: i) the soil was assumed to be normal consolidated; ii) the total stress equal to $\sigma_v = 45$ kPa was taken into account; iii) the air entry value was assumed to remain constant with depth. The water retention behaviour of the soil in the saturated range ($S_r = 1$) was instead expressed by the coefficient of the volumetric compressibility m_v:

$$\frac{\partial \theta}{\partial t} = -m_v \cdot \frac{\partial \sigma'_v}{\partial t} \tag{19}$$

The hydraulic conductivity behaviour was expressed by the Kozeny-Carman equation (Equation (4)) with $k_{sat} = 1.83\text{x}10^{-10}$ m/s and $e_0 = 0.67$, equal to the saturated hydraulic conductivity of the soil in the mock-up scale test.

Numerical results in terms of soil suction, *s* versus distance from the suction drain, *z* are shown in Figure 15. The soil suction at the inner surface of the borehole increases progressively from a negative value (positive pore-water pressure) at day 0 to $s = 15{,}152$ kPa at day 10 of evaporation. The soil suction decreases with distance from the inner surface of the suction drain as expected.

Figure 16 shows the soil water content, *w*, plotted versus distance from the suction drain, *z*. The soil water content decreases over time at the interface with the suction drain and it increases with distance from the surface of the suction drain. These results are consistent with the results in terms of suction.

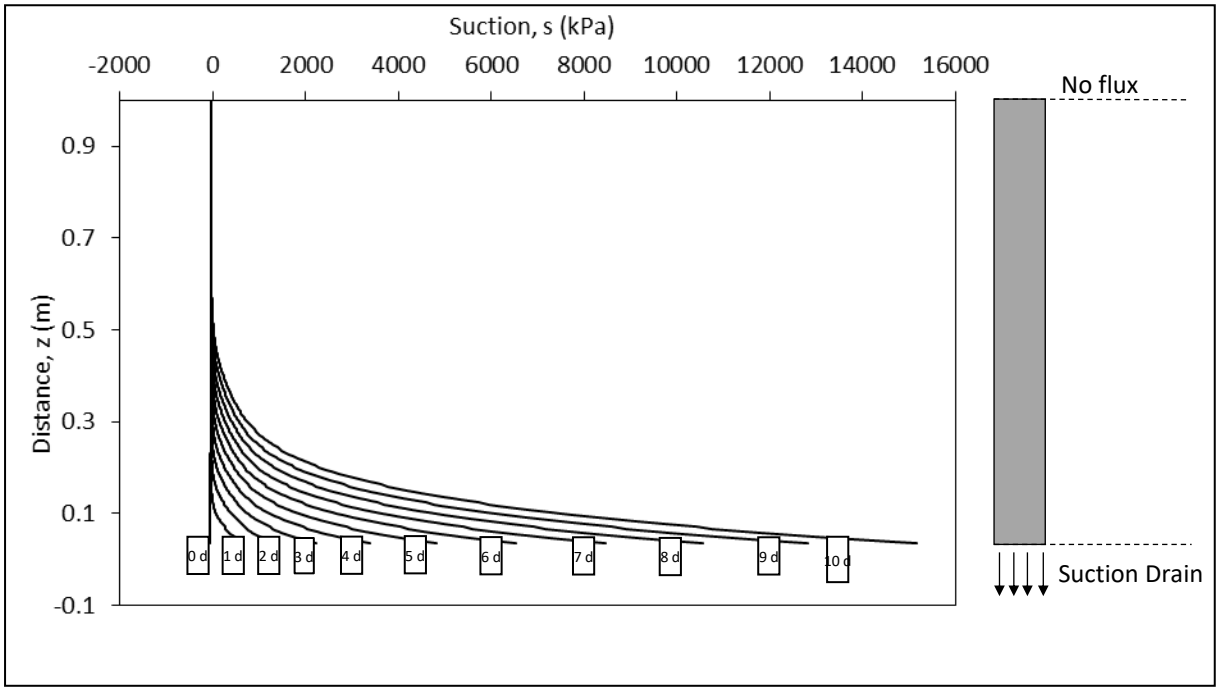

Figure 15: Distribution of the suction, s versus distance from the borehole, z at different time steps

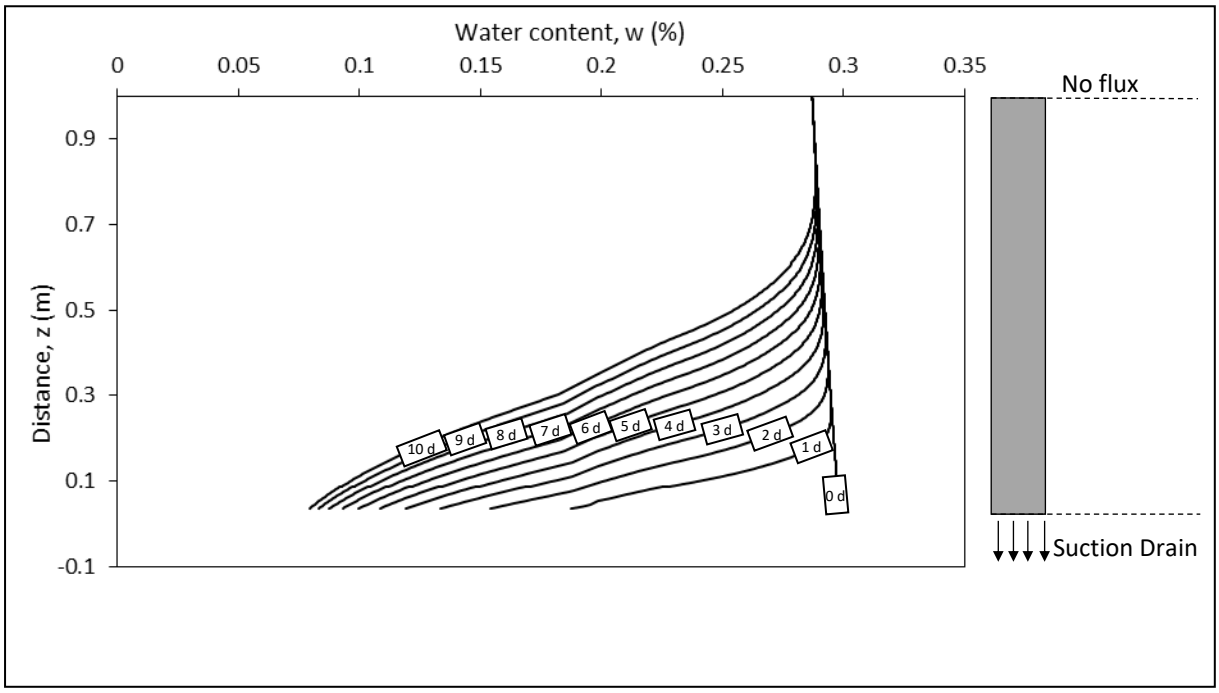

Figure 16: Distribution of the soil water content, w versus distance from the borehole, z at different time steps

The undrained shear strength of soil was calculated as a function of the soil water content by using the equation proposed by (Wroth & Wood, 1978):

$$Cu = 170e^{-4.6I_L} = 1.7 \cdot 10^{2(1-I_L)} \qquad (kPa) \tag{20}$$

where I_L is the liquidity index defined as:

$$\mathrm{I_L} = \frac{\mathrm{w} - \mathrm{w_P}}{\mathrm{w_L} - \mathrm{w_P}} \tag{21}$$

where w is the soil water content, w_P is the plastic limit and w_L is the liquid limit. Equation (21) implies that the undrained shear strength of soil is 1.7 kPa at the limit liquid and 170 kPa at the plastic limit. For the sake of this exercise, the undrained shear strength c_u is assumed to remain constant and equal to 170kPa when the water content drops below the plastic limit $w<w_P$. This is a conservative assumption.

Figure 17 shows the undrained shear strength, c_u versus distance z from the suction drain at different time steps. It is possible to see that c_u is equal to c_u =170kPa at the interface with the suction drain after 1day of evaporation and it decreases with distance from the suction drain.

The longer is the time that the soil is exposed to the evaporation, the larger is the increase in undrained shear strength C_u. At a certain distance from the suction drain, the undrained shear strength recovers the far field profile.

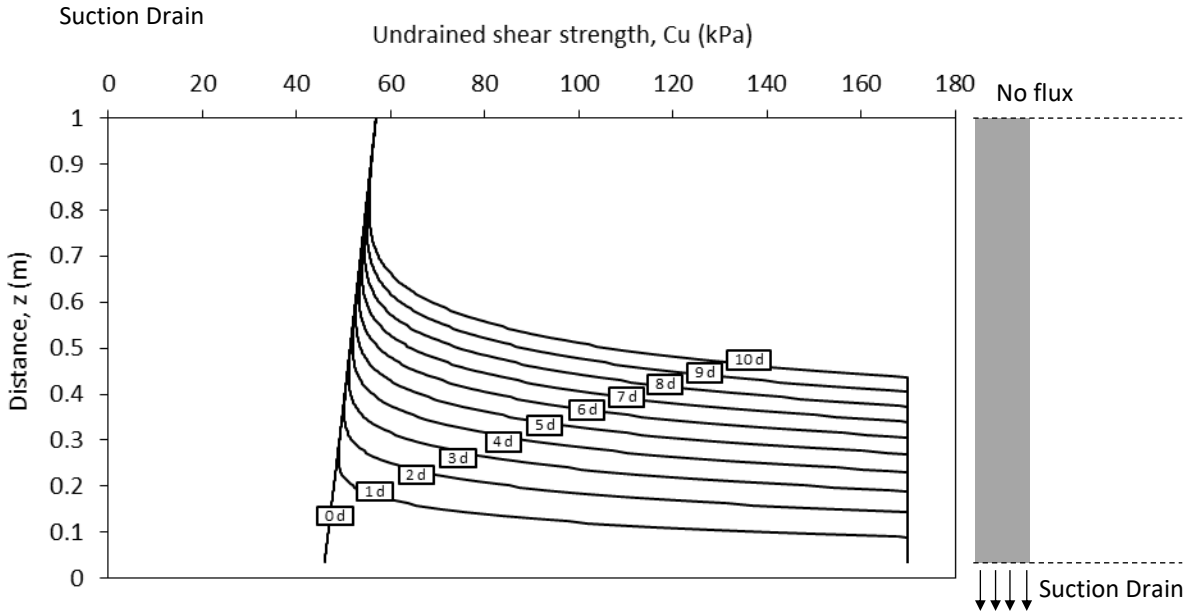

Figure 17: Distribution of the soil undrained shear strength, Cu versus the distance from the borehole, z at different time steps

In order to assess the tunnel face stability by means of Equation (18), a unique value of undrained shear strength has to be selected. The 'equivalent' undrained shear strength $c_{u,eq}$of the soil mass was then calculated according to the following equation:

$$c_{u,eq} = \overline{c_{u,C}}\left(1 - \frac{1}{2\sin^2\alpha}\right) + \overline{c_{u,D}}\left(\frac{1}{2\sin^2\alpha}\right) \tag{22}$$

where $\overline{c_{u,C}}$ and $\overline{c_{u,D}}$ are the average undrained shear strengths of the cover and along the tunnel diameter respectively, and α is one of the angle characterising the kinematically admissible mechanism of failure. As detailed in Appendix III, this angle α is given by

$$\tan\alpha = 2\sqrt{\frac{C}{D} + \frac{1}{4}}; \tag{23}$$

where *C* is the thickness of the cover and *D* is the tunnel diameter.

Eq. (22) was derived under the assumption that the 'equivalent' undrained shear strength should return the same rate of internal dissipation of energy that would occur in a soil mass with non-uniform undrained shear strength. Eq. (22) is fully derived in Appendix III.

The average undrained shear strength along the tunnel diameter $\overline{c_{u,D}}$ is not affected by the suction drains and coincides with the far field undrained shear strength. On the other hand, the average undrained shear strength $C_{u,C}$ of the cover is increased by the suction drains. In this exercise, for sake of simplicity, the undrained shear strength $C_{u,C}$ of the cover was assumed to be equal to the average undrained shear strength in the central layer of the cover between 4m and 5m depth (Figure 13) and was calculated as a first approximation as shown in the window of Figure 18. The average undrained shear strength of the cover versus time, t is plotted in Figure 18. It is possible to observe that the average undrained shear strength $C_{u,C}$ of the cover at the time t=0 day is $C_{u,C}$=51.50kPa and it is more than double at t=10 days. Ultimately, the stability factor N was calculated at different time steps by means of Equations (18) and (22) with a bulk weight of soil taken equal to $\gamma = 20$ KN/m^3, a depth of the cover equal to $C =$ 9m, a tunnel diameter $D = 4$m, and an undrained shear strength of the cover $C_{u,C}$ over time given by Figure 18. The stability factor N over the 10 days of evaporation is shown in Figure 19. The stability factor N decreases from N=4.27 at t=0 day to N=2.79 at t=10 days. Based on the guidelines provided by centrifuge testing (Leca & New, 2007), these results suggest that the tunnel face stability moves from a condition of nearly instability, with ground losses being expected to occur, to a condition of overall ensured stability.

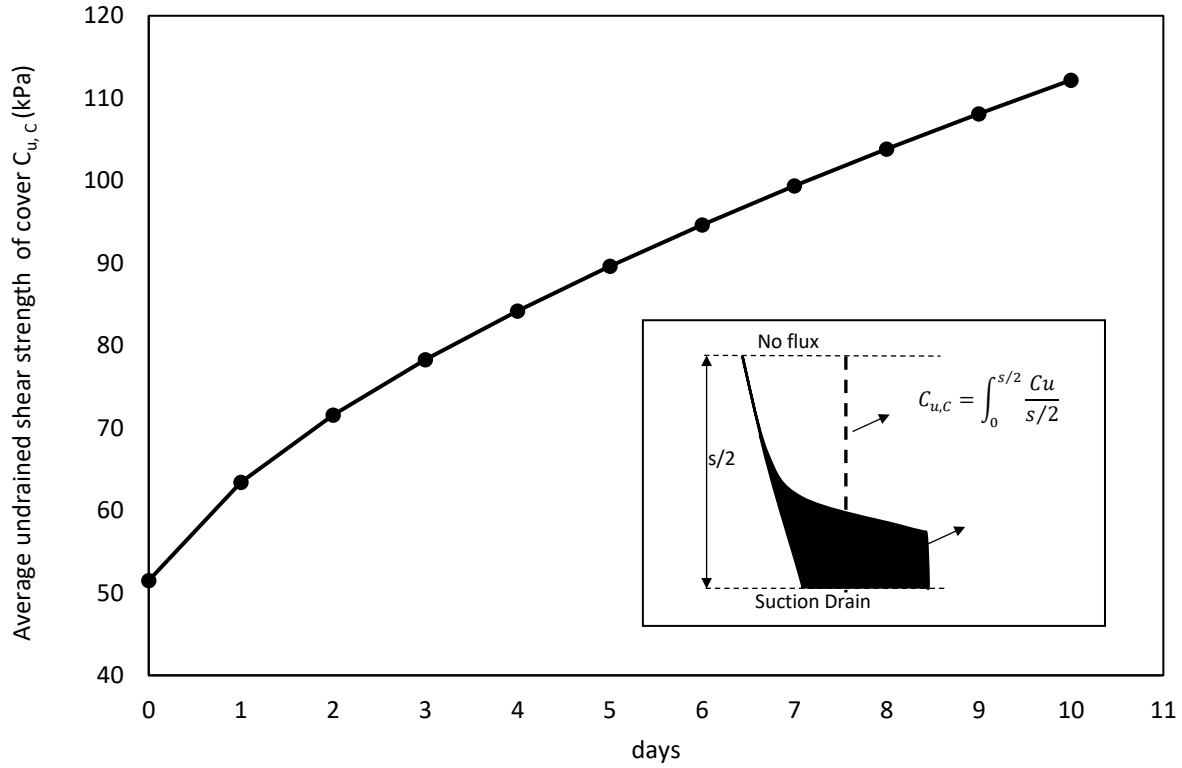

Figure 18: Average undrained shear strength of the cover, $c_{u,C}$ versus time, t

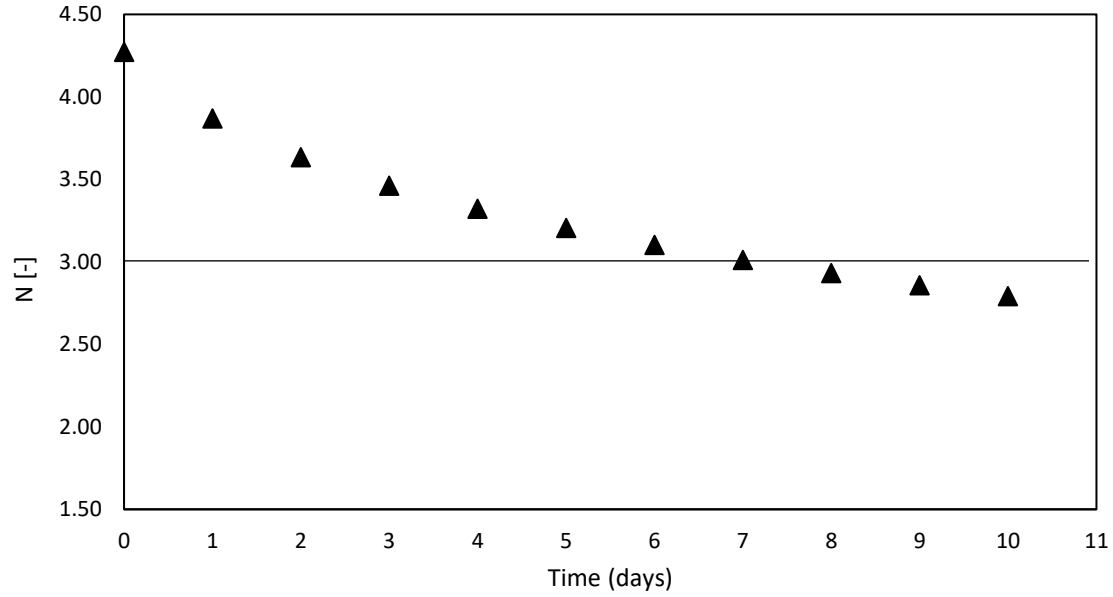

Figure 19: Stability factor, N versus the time of evaporation from the suction drain, t

8 Conclusions

This paper has presented the concept of the suction drain as an innovative technique for temporary stabilisation of geo structures in clayey soils. The concept was validated at laboratory mock-up scale level. A borehole was drilled into a block sample and air was injected to the bottom of the borehole. Airflow circulated from the bottom to the top of the borehole tangentially to the inner surface of the borehole. Experimental results show that the water content of the soil around the borehole decreased significantly. This demonstrated the capacity of the tangential airflow to remove water via evaporation from the soil. The numerical modelling of the mock-up scale test was carried out via a finite element analysis. The agreement between the numerical and the experimental results validated the numerical model as a tool to design suction drains. The suction drain was applied to an ideal case study to demonstrate its effectiveness in enhancing the undrained shear strength and, hence, the tunnel face stability.

The suction drain therefore represents a viable technique for ground improvement that enables the enhancement of the undrained shear strength of clayey soils without using expensive equipment and without leaving spoils into the ground after its application.

9 Acknowledgment

This work was supported by University of Strathclyde, COWI UK and Knowledge Transfer Partnership (KTP) programme (No KTP009575).

10 References

Baroghel-Bouny, V., Mainguy, M. & Coussy, O. (2001). Isothermal drying process in weakly permeable cementitious materials - Assessment of water permeability. Materials Science of Concrete Special Volume: Ion and Mass Transport in Cement-Based Materials, pp. 59-80.

Broms, B. B., & Bennermark, H. (1967). Stability of clay at vertical openings. *Journal of Soil Mechanics & Foundations Div* .

Chapuis, R. P., & Aubertin, M. (2003). On the use of the Kozeny – Carman equation to predict the hydraulic conductivity of soils. *Canadian Geotechnical Journal, 40(3), 616-628*.

Coussy, O. (2004). *Poromechanics*. (West Sussex: Wiley, Ed.).

Davis, E., Gunn, M., Mair, R., & Seneviratine, H. (1980). The stability of shallow tunnels and underground openings in cohesive material. Geotechnique, (4).

Decagon Devices. (2014). WP4C Dew point Potentiameter-Operator's Manual.

Fredlund, D. G., Rahardjo, H., & Rahardjo, H. (1993). *Soil mechanics for unsaturated soils*. (John Wiley & Sons, Ed.).

Leca, E., & New, B. (2007). Settlements induced by tunneling in Soft Ground. *Tunnelling and Underground Space Technology*, *22*(2), 119–149.

Lu, N., & Likos, W. J. (2004). *Unsaturated soil mechanics*. (Wiley, Ed.).

Mair, R. J., & Taylor, R. N. (1997). Theme lecture: Bored tunnelling in the urban environment. In *Theme lecture: Bored tunnelling in the urban environment*. In: Publication Committee of XIV ICSMFE (Eds.), Proceedings of the 14th International Conference on Soil Mechanics & Foundation Engineering, Taylor and Francis,Hamburg, pp. 2353–2385.

Martini, M., & Tarantino, A. (2020). Evaporation-induced soil water flux to design suction drain for low-carbon ground stabilisation. *Tunnelling and Underground Space Technology, in press*.

Mitchell, J. K., & Soga, K. (2005). *Fundamentals of soil behavior*. (New York: John Wiley & Sons, Ed.) (Vol. 3).

Omega Engineering. (2018). User's Guide FMA1000 SERIES.

Tarantino, A., Sacchet, A., Dal Maschio, R. & Francescon, F. (2010). A Hydromechanical Approach to Model Shrinkage of Air-Dried Green Bodies. *Journal of the American Ceramic Society, 93, No. 3, 662–670.*

Tarantino, A. (2009). A water retention model for deformable soils. *Géotechnique, 59, No. 9, 751-762.*

van Genuchten, M. T. (1980). A Closed-form Equation for Predicting the Hydraulic Conductivity of Unsaturated Soils. *Soil Science Society of America Journal, Issue 44, Pp. 892-898*, 892–898.

Wroth, C. P., & Wood, D. M. (1978). The correlation of index properties with some basic engineering properties of soils. *Canadian Geotechnical Journal, 15(2): 137–145.*

APPENDIX I – Anemometer

The sensor design of the anemometer (OMEGA FMA1006R-V2-S) is based on three RTD elements; one measures the air temperature and the other two sensors measure the air velocity. The measurement of the air velocity is based on the heat loss from the RTD velocity sensor as it cools down by the air flow (Omega Engineering, 2018). The specifications of the velocity sensor are summarised in Table A1. The manufacture's calibration of the anemometer was checked against the measurement by a Pitot tube in a wind-tunnel.

Table A1: Specification of the anemometer

Range Air velocity	0-60.96 m/s
Accuracy air velocity	1.5% Full scale range
Display resolution air velocity	0.01m/s
Sensor probe	6.3 OD x 95 mm- 304 Stainless steel
Response time	250 msec default
Operating Relative Humidity	0 to 95% RH without condensation

APPENDIX II – Stress state analysis of thick walled hollow cylinder

This appendix analyses the state of stress in a thick walled hollow cylinder and aims to demonstrate that the rate of change of mean total stress p can be neglected as a first approximation compared to the rate of change of pore-water pressure u_w in the water flow equation (Eqs (8) and (11)). This analysis is limited to the case where the soil is saturated and the principle of effective stress holds. Under these conditions, an analytical solution can be derived and the rate of change of mean total stress can be compared to the rate of change of pore-water pressure u_w analytically.

Consider an element at radius r and defined by an angle increment $d\theta$ (Figure A1). Due to circular symmetry, the circumferential and radial total stresses, σ_θ and σ_r respectively, are functions of r only and not θ. In addition, the shear stresses on the element must be zero. If the ends of the hollow cylinder in vertical direction are open and free, the axial total stress σ_z is also equal to zero if gravity is neglected.

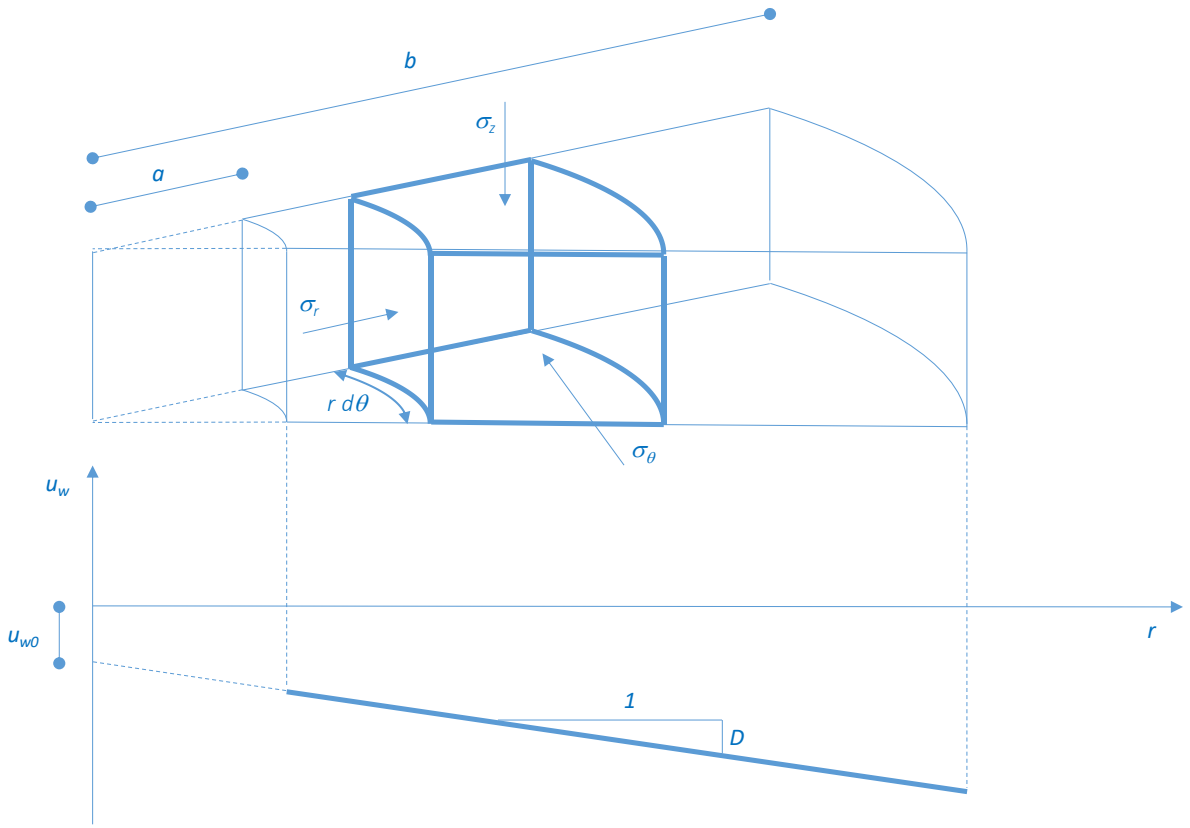

Figure A1. Analytical solution of stress distribution in thick walled hollow cylinder

The equilibrium of the element is written as follows (in terms of total stresses):

$$\frac{d\sigma_r}{dr} + \frac{\sigma_r - \sigma_\theta}{r} = 0 \tag{24}$$

whereas the stress-strain relationships are written in terms of effective stress and take the following form under the assumption of linear elasticity:

$$\begin{aligned} \sigma'_r &= \sigma_r - u_w = (\lambda + 2G)\varepsilon_r + \lambda\varepsilon_\theta \\ \sigma'_\theta &= \sigma_\theta - u_w = \lambda\varepsilon_r + (\lambda + 2G)\varepsilon_\theta \end{aligned} \tag{25}$$

where λ is the Lamé's first modulus, G is the shear modulus, ε_r and ε_θ are the radial and circumferential strains respectively, u_w is the pore-water pressure, and σ'_θ and σ'_r are the circumferential and radial effective stresses respectively.

The elastic parameters are linked with the Young's modulus E and the Poisson's ratio ν via the following equations:

$$\begin{aligned} \lambda &= \frac{E\nu}{(1+\nu)(1-2\nu)} \\ G &= \lambda\frac{1-2\nu}{2\nu} = \frac{E\nu}{(1+\nu)(1-2\nu)}\frac{1-2\nu}{2\nu} = \frac{E}{2(1+\nu)} \end{aligned} \tag{26}$$

The total stresses can be derived from Eq. (26) as follows:

$$\begin{aligned} \sigma_r &= (\lambda + 2G)\varepsilon_r + \lambda\varepsilon_\theta + u_w \\ \sigma_\theta &= \lambda\varepsilon_r + (\lambda + 2G)\varepsilon_\theta + u_w \end{aligned} \tag{27}$$

and the radial and circumferential strains are liaised with the radial displacement u via the following relationships:

$$\varepsilon_r = \frac{du}{dr}$$
$$\varepsilon_\theta = \frac{u}{r} \tag{28}$$

By replacing Eqs. (27) and (28) into Eq. (24), the governing differential equation can be derived:

$$(\lambda + 2G)\frac{d}{dr}\left(\frac{du}{dr} + \frac{u}{r}\right) + \frac{du_w}{dr} = 0 \tag{29}$$

Let us assume that the pore-water pressure is distributed linearly along the radius *r* (Figure A1) and is therefore characterised by:

$$u_w = u_{w_0} + Dr \tag{30}$$

The governing equation therefore has the following solution:

$$u = Ar + \frac{B}{r} - \frac{D}{3(\lambda + 2G)}r^2 \tag{31}$$

where *A* and *B* are constants to be determined from the mechanical boundary conditions and u_{w0} ad *D* are the intercept and slope of the linear pore-water pressure distribution respectively. According to Eqs. (31), the radial and circumferential total stresses can be re-written as follows:

$$\sigma_r = 2A(\lambda + G) - 2G\,\frac{B}{r^2} + \frac{1}{3}Dr\left(\frac{2G}{\lambda + 2G}\right) + u_{w_0}$$
$$\sigma_\theta = 2A(\lambda + G) + 2G\frac{B}{r^2} + \frac{2}{3}Dr\left(\frac{2G}{\lambda + 2G}\right) + u_{w_0} \tag{32}$$

Imposing the mechanical boundary conditions at the inner and outer radii of the hollow cylinder, *a* and *b* respectively, we have:

$$\sigma_r(b) = 0$$
$$\sigma_r(a) = 0 \tag{33}$$

the following expressions are derived for the parameters A and B

$$A = \frac{1}{2(\lambda + G)}\left[-\frac{D}{3}\left(\frac{a^2}{b+a} + b\right)\left(\frac{2G}{\lambda + 2G}\right) - u_{w0}\right]$$
$$B = -\frac{D}{3}\left(\frac{1}{\lambda + 2G}\right)\frac{a^2 b^2}{b+a} \tag{34}$$

By replacing Eqs. (34) into Eqs. (32), the following equation is derived for the total mean stress p:

$$p = \frac{\sigma_\theta + \sigma_r + \sigma_z}{3} = \frac{1}{3}\left(\frac{2G}{\lambda + 2G}\right)\left[-\frac{2}{3}\left(\frac{a^2}{b+a} + b\right) + r\right]D \tag{35}$$

According to Eqs. (26), one can write

$$\frac{2G}{\lambda + 2G} = \frac{1 - 2\nu}{1 - \nu} \tag{36}$$

and the equation for the mean total stress can be finally written as

$$p = \frac{\sigma_\theta + \sigma_r + \sigma_z}{3} = \frac{1}{3}\left(\frac{1 - 2\nu}{1 - \nu}\right)\left[-\frac{2}{3}\left(\frac{a^2}{b+a} + b\right) + r\right]D \tag{37}$$

The rate of change of mean total stress p and the rate of change of pore-water pressure u_w can now be calculated by deriving Eqs. (30) and (37) with respect to time:

$$\frac{\partial p}{\partial t} = \frac{\sigma_\theta + \sigma_r + \sigma_z}{3} = \frac{1}{3}\left(\frac{1 - 2\nu}{1 - \nu}\right)\left[-\frac{2}{3}\left(\frac{a^2}{b+a} + b\right) + r\right]\frac{\partial D}{\partial t}$$
$$\frac{\partial u_w}{\partial t} = \frac{\partial u_{w0}}{\partial t} + r\frac{\partial D}{\partial t} \tag{38}$$

By combining Eqs. (38), the rate of change of mean total stress p can be expressed as a fraction of the rate of change of pore-water pressure u_w as follows:

$$\frac{\partial p}{\partial t} = \underbrace{\frac{1}{3}\frac{1-2\nu}{1-\nu}\left[-\frac{2}{3}\left(\frac{a^2}{b+a}+b\right)+r\right]\frac{1}{r}}_{K_{p,u_w}}\left(\frac{\partial u_w}{\partial t}\right) + \frac{1}{3}\frac{1-2\nu}{1-\nu}\left[-\frac{2}{3}\left(\frac{a^2}{b+a}+b\right)+r\right]\frac{1}{r}\left(-\frac{\partial u_{w0}}{\partial t}\right) \quad (39)$$

Eq. (39) include two terms on the right-hand side. The first term allows comparing the rate of change of mean total stress p with the to the rate of change of pore-water pressure u_w. The coefficient in the first term on the right-hand side is plotted against the radius r in Figure A2. It shows that the $\frac{\partial p}{\partial t}$ is different from zero but is relatively small compared to $\frac{\partial u_w}{\partial t}$. The time derivative in the second term has negative sign, which makes the actual $\frac{\partial p}{\partial t}$ smaller than the value predicted by the first term, i.e. the coefficient $K_{p,uw}$ plotted in Figure A2. Overall, this justifies the assumption that the variation of the total stress $\partial p/\partial t$ can be assumed to be negligible in comparison to the variation of the pore water pressure $\partial u_w/\partial t$.

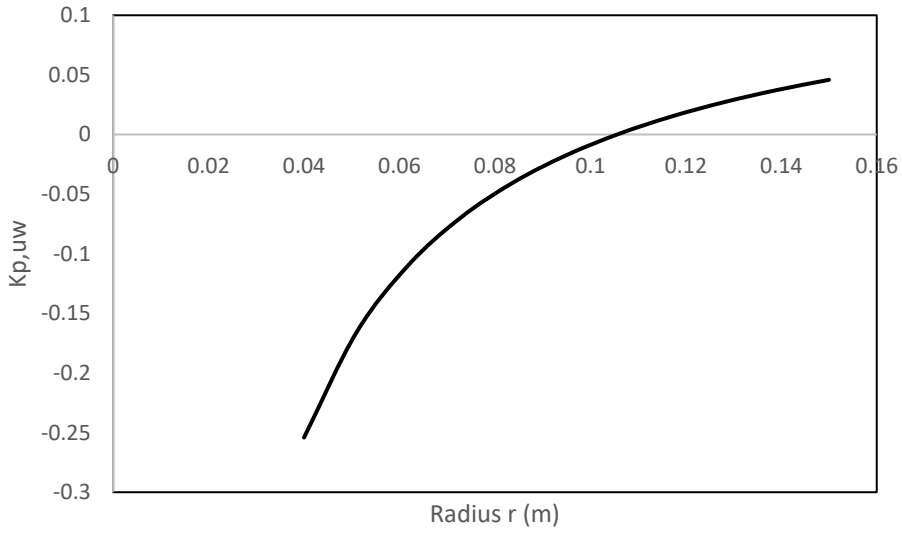

Figure A2. Ratio between change of mean total stress p with respect to the rate of change of pore-water pressure u_w.

APPENDIX III – Equivalent undrained shear strength

Undrained shear strength is generally assumed to be constant in the stability analysis of the tunnel face. However, the suction drains modify significantly the undrained shear strength in the tunnel cover and the undrained shear strength is therefore no longer uniform in the soil mass. To derive a single 'equivalent' undrained shear strength for the stability analysis of the tunnel face within the framework, one can refer to solution derived within the framework of the upper bound theorem of plasticity (Davis et al 1980).

Stability of the tunnel face is controlled by the rate of internal dissipation of energy W_i along the failure surfaces associated with a kinematically admissible two-block mechanism illustrated in Figure A3a. This is given by

$$W_i = \overline{c_{u,AF'}} L_{AF'} \delta_1 + \overline{c_{u,F'B}} L_{F'B} \delta_1 + \overline{c_{u,FG}} L_{GF} \delta_1 + \overline{c_{u,BE}} L_{BE} \delta_2 + \overline{c_{u,BF}} L_{BF} \delta_{21} \quad (40)$$

where $\overline{c_{u,AF'}}$, $\overline{c_{u,F'B}}$, $\overline{c_{u,FG}}$, $\overline{c_{u,BE}}$, and $\overline{c_{u,BF}}$ are the average undrained shear strengths along the segments having length $L_{AF'}$, $L_{F'B} L_{FG}$, $L_{BE} \delta_2$ and L_{BF} respectively, δ_1 and δ_2 are the absolute displacements of the two blocks respectively, and δ_{21} is the relative displacement between the two blocks.

The equivalent undrained shear strength $c_{u,eq}$ can be defined as the uniform shear strength that returns the same rate of internal dissipation of energy

$$W_i = c_{u,eq} (L_{AF'} \delta_1 + L_{F'B} \delta_1 + L_{FG} \delta_1 + L_{BE} \delta_2 + L_{BF} \delta_{21}) \quad (41)$$

By equating Eqs. (40) and (41), the equation for the equivalent undrained shear strength can be derived as follows:

$$c_{u,eq} = \frac{\overline{c_{u,AF'}} L_{AF'} \delta_1 + \overline{c_{u,F'B}} L_{F'B} \delta_1 + \overline{c_{u,FG}} L_{GF} \delta_1 + \overline{c_{u,BE}} L_{BE} \delta_2 + \overline{c_{u,BF}} L_{BF} \delta_{21}}{L_{AF'} \delta_1 + L_{F'B} \delta_1 + L_{FG} \delta_1 + L_{BE} \delta_2 + L_{BF} \delta_{21}} \quad (42)$$

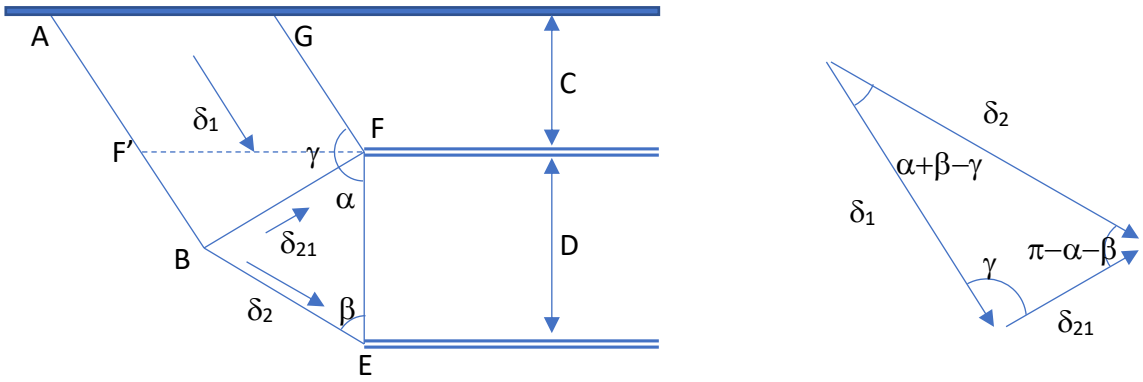

(a) (b)

Figure A3. (a) Two- block kinematically admissible mechanism. (b)| Displacement odogram

The absolute displacements of the two blocks, δ_1 and δ_2 respectively, and the relative displacement δ_{21} can be derived from the displacement odogram in Figure A3b:

$$\delta_2 = \delta_1 \frac{\sin\gamma}{\sin(\alpha+\beta)}$$
$$\delta_{21} = \delta_1 \frac{\sin(\alpha+\beta-\gamma)}{\sin(\alpha+\beta)} \quad (43)$$

The geometry of the blocks is characterised by:

$$L_{AB} = L_{AF'} + L_{F'B} = \frac{C}{\cos(\pi-\alpha-\gamma)} + \frac{\frac{D}{2}}{\cos(\pi-\alpha-\gamma)}$$
$$L_{GF} = \frac{C}{\cos(\pi-\alpha-\gamma)} \quad (44)$$
$$L_{BF} = \frac{D}{2\cos\alpha}$$
$$L_{BE} = \frac{D}{2\cos\beta}$$

Let us consider the soil mass represented by two values of shear strength, $\overline{c_{u,C}}$ and $\overline{c_{u,D}}$, associated with the average undrained shear strengths of the cover and along the tunnel diameter respectively. We can write:

$$\overline{c_{u,AF'}} = \overline{c_{u,FG}} = \overline{c_{u,C}}$$

$$\overline{c_{u,F'B}} = \overline{c_{u,BE}} = \overline{c_{u,BF}} = \overline{c_{u,D}} \tag{45}$$

According to Davis et al (1980), the upper bound solution is minimised for

$$\alpha = \beta \; and \; \gamma = \frac{\pi}{2} \tag{46}$$

with

$$\tan\alpha = 2\sqrt{\frac{C}{D} + \frac{1}{4}}; \tag{47}$$

where C is the thickness of the cover and D is the tunnel diameter.

By replacing Eqs. (43) and (46) into Eq. (42), an expression for the equivalent undrained shear strength can be derived :

$$c_{u,eq} = \overline{c_{u,C}} \underbrace{\left(1 - \frac{1}{2\sin^2\alpha}\right)}_{K_C} + \overline{c_{u,D}} \underbrace{\left(\frac{1}{2\sin^2\alpha}\right)}_{K_D} \tag{48}$$

It is interesting to plot the coefficients K_C and K_D weighing the undrained shear strengths associated with the two regions, C and D respectively (Figure A4). At low values of the ratio C/D (shallow tunnels), the undrained shear strength along the tunnel diameter dominates the equivalent shear strength, i.e. the increase in undrained shear strength generated by the suction drains in the cover has a marginal effect on the 'equivalent' undrained shear strength and, hence, on the stability of the tunnel face. On the other hand, for relatively high values of the ratio C/D, the undrained shear strength in the cover (affected by the suction drains) becomes as important as the undrained shear strength along the tunnel in controlling the equivalent shear strength.

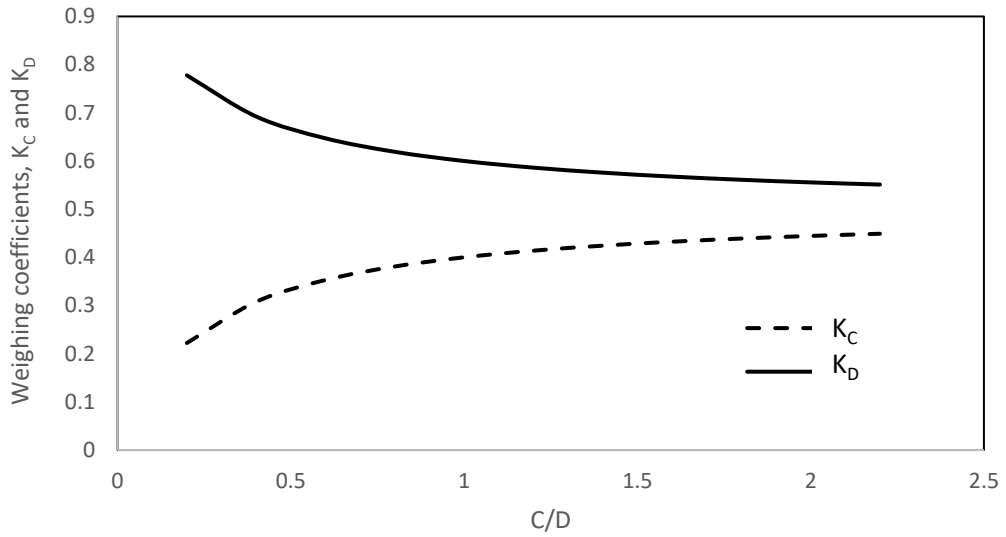

Figure A4. Weighing coefficients for undrained shear strengths of the cover, $\overline{c_{u,C}}$, and along the tunnel diameter, $\overline{c_{u,D}}$.